Is SmB_6 a Topological Insulator?

by

©Khawla Elfied

A thesis submitted to the School of Graduate Studies in partial fulfillment of the requirements for the degree of

Master of Science (Physics)

Department of Physics and Physical Oceanography
Memorial University of Newfoundland

Memorial University of Newfoundland

April 2017

ST. JOHN'S NEWFOUNDLAND

Abstract

We examined whether samarium hexaboride (SmB_6) is a topological insulator, or not by reviewing and reanalyzing all published experimental results to date. Despite the fact that the SmB_6 has long been known as a Kondo insulator, with strong correlations and band hybridization, it is still of great interest because of low-temperature transport anomalies which have recently been interpreted as evidence that SmB_6 is a topological insulator. SmB_6 behaves electronically at high temperature like an insulator, and at low temperature its resistance mysteriously saturates.

We studied de Haas van-Alphen quantum oscillation results to resolve the Fermi surface topology in this material. Although dHvA measurement may be consistent with two-dimensional conducting electronic states, we find an elongated 3D ellipsoidal Fermi surface is also consistent with the experimental results. Furthermore, resistance measurements also can give some evidence of SmB_6 surface conductivity, by studying different geometries to determine whether the conduction is dominated by the surface or the bulk. Also, We simulated the conductivity of a thin sample to assess whether the experimental measurements on their sample are consistent with surface conductivity.

After analyzing these experiments and others, our conclusion is that the main experimental results can be described as either bulk or surface conduction, but resistivity measurements strongly suggest surface conduction. Even if further studies prove the surface conductivity, further studies will be required to show that SmB_6 is

a topological material.

Acknowledgements

All my appreciation to my Lord GOD Allah, for his beautiful designing of my life.

In the first place, I would like to thank my mother, Mrs. Noriya, and my father, Mr. Khairy for all they have done for me, their love and support mean more to me than they will ever know. Also, I sincerely wish to thank my siblings for their wonderful support.

I gratefully acknowledge the opportunity to work with Professor Stephanie Curnoe, and I would like to thank her for her assistance and advice during my MSc study.

I am unable to fully express my gratitude for the support of my husband, Mr. Ahmad Zaied. If I have been able to accomplish anything these past few years it is only because of his sacrifices, which enabled me to walk through challenges. Also, I would thank my dearest daughters for being in my life, without them, I would be nowhere near the person I am – and the person I am still working on becoming. There are not enough words in the world to express my appreciation.

Finally, I would like to acknowledge the Libyan ministry of higher education and CBIE for supporting my MSc study.

To my lovely daughters(Tasnim and Tuqa),

for their loving support.

Table of Contents

List of Tables

List of Figures

Chapter 1

Introduction

Topological insulators are materials that exhibit a qualitatively new aspect of quantum mechanics. Topological insulators are insulators in bulk but have gapless surface states which conduct. These gapless states must exist due to the topology of the band structure. Several dozens of such materials have been discovered, but most of them are weakly correlated band insulators. Samarium hexaboride a strong correlated Kondo insulator was proposed to be a 3D topological insulator in 2011 [6]. In this work, we examined whether samarium hexaboride is a topological insulator, or not by reviewing and reanalyzing all published experimental results to date.

In quantum mechanics, the state of a system is described by linear combinations of orthonormal vectors forming a basis set, and this orthonormal basis spans the Hilbert space, which is a linear vector space. It is topological when the Hilbert space has a non-trivial topology. Then, we can find different kinds of topological insulators depending on the topology of the Hilbert space. The non-trivial topology is a feature of gapped energy states, and as long as the energy gap remains open, the topology cannot change. However, because of the potential that confines electrons within the sample, there will be gapless states at the boundary. Thus, two-dimensional topological insulators are

related to gapless edge states. Likewise, three-dimensional topological insulators are connected to gapless surface states [4].

In 1980, the quantum Hall (QH) state was discovered, and it is now understood to be an example of a topological insulator [3]. The quantum Hall effect happens at low temperature and high magnetic field. The electrons in the bulk move in cyclotron orbits with the radius depending on the magnitude of the applied magnetic field. However, electrons near the edge move in semi-circle paths along the edge. This gives the idea how electrons in bulk cannot carry current, and the electrons near the surface do.

1.1 History of topological insulators

Before 1980, in condensed matter systems, all states of matter could be classified by the principle of broken symmetry. The discovery of quantum Hall (QH) states in 1980 was the first example of a quantum state that depends only on topology. Thus, this class has no broken symmetry. Subsequently, another new topological class has arisen which is called Quantum Spin Hall (QSH) states or topological insulator. The main difference between QH states and QSH states is that QH states need an external magnetic field which breaks time reversal symmetry while QSH states are time reversal (TR) invariant. Both cases (QH) and (QSH) have been experimentally observed [3].

1.1.1 Integer quantum Hall effect

The quantum Hall system, the first known topological insulator, is due to the Landau quantization. In a 2D system, the electronic spectrum is a set of highly degenerate "Landau levels" with energy $\left(\nu + \frac{1}{2}\right) w_c$, where $w_c = \frac{eB}{mc}$ is the cyclotron frequency and ν is an integer. When the chemical potential lies between Landau levels, the

longitudinal conductivity vanishes, and the Hall conductivity is $\frac{\nu e^2}{h}$,

$$\sigma = \begin{bmatrix} 0 & -\nu\frac{e^2}{h} \\ \nu\frac{e^2}{h} & 0 \end{bmatrix}, \tag{1.1}$$

where e is a charge of the electron, h is Planck's constant and ν is the number of filled Landau levels. It is important to note that quantum Hall states explicitly breaks time reversal (TR) symmetry due to the magnetic field. In 1985, Von Klitzing was awarded the Nobel Prize in physics for discovering that the Hall conductivity σ_{xy} was exactly quantized to integer multiples of $\frac{e^2}{h}$. This quantization of Hall conductance is now known as a topological invariant. It was shown by Thouless, Kohmoto, Nightingale, and den Nijs (TKNN) in 1982 that this effect is not only quantum mechanical but also is a new topological phenomenon. The TKNN invariant ν is now known as the first Chern number.

1.1.2 Quantum Spin Hall effect

A new topological class of materials called the quantum spin Hall effect (QSHE) was theoretically predicted in 2006 by Bernevig and Zhang [22] and experimentally observed by Koenig et al. in 2007 [17], and Roth et al. in 2009 [25]. The QSHE occurs in 2D topological insulators that are invariant under time reversal (TR), and spin-orbit coupling plays a fundamental role. The QSHE is essentially two time-reversed copies of the quantum Hall insulator. Their charge currents cancel, but the spin current is quantized. It is called a quantum spin Hall insulator with spin conductance equal to $\frac{2e^2}{h}$. Kane and Mele (2005) [24] recognized that the electronic states of the QSH insulator are described by a new topology given by a Z_2 index. Z is the set of integers and Z_2 is the quotient group which classifies even or odd integers. In conventional

insulators, $Z_2 = +1$ (even), but reverses sign in topological insulators, $Z_2 = -1$. The index Z_2 is determined by the number of edge states which cross the Fermi level [21].

1.1.2.1 Mercury Telluride HgTe quantum wells

The first two-dimensional topological insulator was predicted to occur in mercury cadmium telluride (HgTe/CdTe) quantum wells in 2006 by Bernevig, Hughes, and Zhang (BHZ) [23]. The fundamental property of HgTe is band inversion where the s and p levels at the conduction and valence band edges are interchanged compared to normal insulator such as CdTe. In the HgTe, the band gap is smallest near the Γ point ($\vec{k} = 0$) in the Brillouin zone. BHZ showed that the HgTe layer exhibits an inverted band structure, for an appropriate range of well thickness (when the well thickness d is greater than a certain critical thickness d_c). For thickness $d < d_c$ (thin HgTe layer) the band structure is in the normal state, while for the thickness $d > d_c$ (thick HgTe layer), the band structure is in the inverted system. At $d = d_c$, the gap closes at the Γ point. Because of time reversal symmetry and Kramers' theorem, both bands are doubly degenerate. [23] gives the most general model describing these two bands system

$$H = \begin{pmatrix} H(\vec{k}) & 0 \\ 0 & H^*(-\vec{k}) \end{pmatrix}, \tag{1.2}$$

where

$$H(\vec{k}) = \epsilon(\vec{k}) + d_i(\vec{k})\sigma_i. \tag{1.3}$$

$$d_1 = Ak_x, \tag{1.4}$$

$$d_2 = Ak_y, \tag{1.5}$$

$$d_3 = M - B(k_x^2 + k_y^2), \tag{1.6}$$

$$\epsilon(\vec{k}) = C - D(k_x^2 + k_y^2) \tag{1.7}$$

and A, B, C, D, and M are model parameters. The term $d_i(\vec{k})\sigma_i$ is due to spin orbit coupling. At the Γ point, the energy eigenvalues are $\epsilon(0) \pm M$. M varies with the well thickness; $M = 0$ at $d = d_c$, so M changes sign between the two sides of the transition ($+M$ at $d < d_c$ and -M at $d > d_c$) and the bands reverse. In either situation, we have a doubly degenerate filled band, separated by a doubly degenerate vacant band. Time reversal symmetry ensures that the Hall conductance vanishes, there is a cancellation between the contributions of filled bands. However, the spin Hall conductance vanishes when $M > 0$, but is $\sigma_{xy}^{(s)} = \dfrac{2e^2}{h}$ for $M < 0$. Both the spin and electrical conductances are calculated using Berry's phases, as we shall explain in Section 1.2.

1.1.3 Three-dimensional (3D) topological insulators

Later on, theoretical groups (Fu and Kane [26]; Fu et al [11]; Kane and Mele [24]; Moore and Balents [27]; Qi et al [8]; Roy [14]) extended the concept of 2D to 3D topological insulators. Moore and Balents [27], L. Fu, C. Kane and E. Mele [11], and R. Roy [14] discovered that three-dimensional insulators can obtain a topological order through a spin-orbit driven band inversion, similar to HgTe in 2D. They showed that in a three-dimensional topological insulator there are four Z_2 topological numbers, $(\nu_0; \nu_1, \nu_2, \nu_3)$. Where the ν_0 is the most important number, because it gives the distinction between a strong and weak topological insulators, while the other topological numbers provide information on dispersion and topology of the Fermi surfaces of surface states. When $\nu_0 = 1$, a 3D TI is called a " strong topological insulator", in which gapless surface states exist on every surface. On the other hand, it is called weak topological insulator when $\nu_0 = 0$ and gapless states may

be absent on some surfaces [3, 4, 6, 20].

The first topological insulator, discovered in 2008 by R. Cava and Z. Hasan [28], was bismuth antimonide ($Bi_{1-x}Sb_x$). As well, Bi_2Te_3 and Sb_2Te_3 were theoretically predicted as 3D topological insulators [15], and also Bi_2Se_3 [15,28]. In 3D topological insulators, when time-reversal symmetry is broken by a magnetic field, the surface states become quantum Hall states with $\sigma_{xy} = \pm\frac{1}{2}\frac{e^2}{h}$ [3].

In this work, we are interested in SmB_6, which is a very interesting 3D topological insulator candidate with the Z_2 invariants equal to (1;1, 1, 1). If it is indeed a topological insulator, it will be the first material where both electron correlations and non-trivial band topology play important role [4].

1.2 Basics of Topology in Topological insulators

1.2.1 Berry phase

The Berry phase is important in the discussions of topological insulator; as we shall explain, the Hall conductance can be calculated using Berry phase. In 1984, Michael Berry [1, 4] discovered that a quantum system adiabatically transported around a closed path in the space of external parameters acquires a phase that depends only on the geometry of the circuit.

Let us consider a quantum-mechanical system described by a Hamiltonian $H(R)$, where $R = (R_1, R_2, R_3, ...)$ is an external parameter (for example, a magnetic field). The parameter $R(t)$ is varied slowly with time. Thus the Schrödinger equation takes the form:

$$H(R)|n(R)\rangle = E_n(R)|n(R)\rangle, \tag{1.8}$$

where $|n(R)\rangle$ are eigenstates of $H(R)$.

In order to analyze the phase of the system, we assume that the initial state is a pure state $|n(R(0))\rangle$ and we slowly vary $R(t)$ with time. The phase $\theta(t)$ of the state $|\psi(t)\rangle = e^{-i\theta(t)}|n(R(t))\rangle$ during the adiabatic evolution will contain more than the dynamical phase. Thus, the time evolution of the system is governed by:

$$H(R(t))|\psi(t)\rangle = i\hbar\frac{d}{dt}|\psi(t)\rangle; \tag{1.9}$$

also we have

$$H(R(t))|n(R(t))\rangle = E_n(R(t))|n(R(t))\rangle, \tag{1.10}$$

therefore have

$$E_n(R(t))|n(R(t))\rangle = \hbar\left(\frac{d}{dt}\theta(t)\right)|n(R(t))\rangle + i\hbar\frac{d}{dt}|n(R(t))\rangle; \tag{1.11}$$

and since $\langle n(R(t))|n(R(t))\rangle = 1$, we find

$$E_n(R(t)) = \hbar\left(\frac{d}{dt}\theta(t)\right) + i\hbar\langle n(R(t)|\left(\frac{d}{dt}|n(R(t))\rangle\right) \tag{1.12}$$

hence, the phase $\theta(t)$ is given by:

$$\theta(t) = \frac{1}{\hbar}\int_0^t E_n(R(t'))dt' + \gamma_n(t) \tag{1.13}$$

where

$$\gamma_n(t) = -i\int_0^t dt'\langle n(R(t')|\left(\frac{d}{dt'}|n(R(t'))\rangle\right) \tag{1.14}$$

The first term in $\theta(t)$ is the usual dynamic phase while the second term $\gamma_n(t)$ is the Berry phase.

When R is a vector quantity (such as the components of a magnetic field), it is

useful to define a vector potential $\vec{A}_n(R)$

$$\vec{A}_n(R) = i\langle n(R)|\Big(\vec{\nabla}_R|n(R)\rangle\Big) \tag{1.15}$$

so that

$$\gamma_n = \int_C dR \cdot \vec{A}_n(R), \tag{1.16}$$

where C is a path through the parameter space of $\vec{R}$, and the endpoints are $\vec{R}(0)$ and $\vec{R}(t)$. $\vec{A}_n(R)$ is called the Berry vector potential. If the path is closed this line integral can be transformed to a surface integral via Stokes theorem,

$$\gamma_n = -i \int dS_i \epsilon_{ijk} F_{jk}, = -i \int dS \cdot \vec{B} \tag{1.17}$$

where $F_{jk} = \partial_j A_k - \partial_k A_j$ is the Berry curvature and $B_i = \epsilon_{ijk} F_{jk}$. Thus an integral over a closed surface depends on singularities of B inside the surface.

The integral of the Berry curvature over the full 2D Brillouin zone of all filled bands is the Hall conductance σ_{xy},

$$\sigma_{xy} = -i\frac{e^2}{h} \int \frac{dk_x dk_y}{(2\pi)^2} \sum_{a=1}^{m} F^a_{xy}(k), \tag{1.18}$$

where m is number of filled bands and the Berry curvature is:

$$F^a_{xy} = \partial k_x \langle a,k|(\partial k_y|a,k\rangle) - \partial k_y \langle a,k|(\partial k_x|a,k\rangle) \tag{1.19}$$

$$= (\partial k_x \langle a,k|)(\partial k_y|a,k\rangle) - (\partial k_y \langle a,k|)(\partial k_x|a,k\rangle) \tag{1.20}$$

$|a,k\rangle$ represents a state with momentum k in the a^{th} band. Because it depends only on singularities in the curvature and not on details of the band structure, it is a topological invariant (the Chern number, ν).

1.2.2 Time reversal

Time reversal is defined as reversal of direction of motion, $T\hat{P}T^{-1} = -\hat{P}$, while it leaves the position operator $\hat{X}$ unchanged $T\hat{X}T = X$. Therefore, it also reverses the sign of angular momentum $\hat{L}$

$$T\hat{L}T^{-1} = -\hat{L} \tag{1.21}$$

and spin $\hat{S}$

$$T\hat{S}T^{-1} = -\hat{S}. \tag{1.22}$$

The TR operator is an anti-unitary operator which can be written in the form:

$$T = UK, \tag{1.23}$$

where K is complex conjugation and U is a unitary operator.

When the time reversal operator is applied twice the result must return to the original state

$$T^2 = UKUK = UU^* = U(U^T)^{-1} = \phi\mathbf{1} \tag{1.24}$$

where ϕ is a phase and that equals to ± 1. The case of $T^2 = 1$ applies to particle with integer spin. On the other hand, in case of spin $\frac{1}{2}$ particles, $T^2 = -1$. This leads Kramers' theorem, which states that for systems of $\frac{1}{2}$ integer spin, all states are doubly degenerate (Kramers' degeneracy).

Time reversal symmetry guarantees that the Hall conductance vanishes. This is due to a cancellation between the current contributions of the two spin components. In the spin conductance, instead of canceling, these contributions add, giving a quantized spin Hall conductance.

1.3 Summary

In this chapter, we present some information about the phenomena of topological insulators, and we review the first two-dimensional topological insulators (predicted in mercury cadmium telluride (HgTe/CdTe), as well as some physical phenomena that are related to this topic. The rest of this Thesis is organized as follows: in Chapter 2, we will discuss aspects of samarium hexaboride (SmB_6) and review its band structure. Chapter 3 and Chapter 4 are devoted to examining SmB_6 by reanalyzing previously published experimental studies of de Haas van-Alphen quantum oscillations [45] and resistivity [55]. As well, we simulated the conductivity of a thin sample to assess whether the experimental measurements on their sample are consistent with surface conductivity. In Chapter 5 and Chapter 6, we present the discussion and the conclusion of whether samarium hexaboride (SmB_6) is a topological insulator or not.

Chapter 2

Samarium hexaboride

2.1 What is samarium hexaboride ?

Samarium hexaboride (SmB_6) is one of the rare earth hexaborides (RB_6) that have been studied for many decades. It was discovered more than fifty years ago by Anthony Menth, Ernest Buehler, and Ted Geballe [43]. SmB_6 is known to be a "Kondo insulator" -a classical mixed valence narrow gap semiconductor with a large effective mass. The hybridization between localized f-electrons and conduction bands leads to very narrow band gap opening, as shown in Figure 2.1, which makes it difficult to observe clear in-gap states near the Fermi level.

SmB_6 is a paramagnetic metal at room temperature, with a Curie-Weiss susceptibility characteristic of magnetic Sm^{+3} ions. Below 50 K, it changes into a paramagnetic insulator with a small (10 meV) gap. However, there is a low-temperature resistivity plateau, which is the significant property that brings researchers' interest to study SmB_6. This behavior may indicate the existence of surface conductivity, as in a topological insulator.

As recently as 2010, M. Dzero, K. Sun, V. Galitski, and P. Coleman [30] proposed

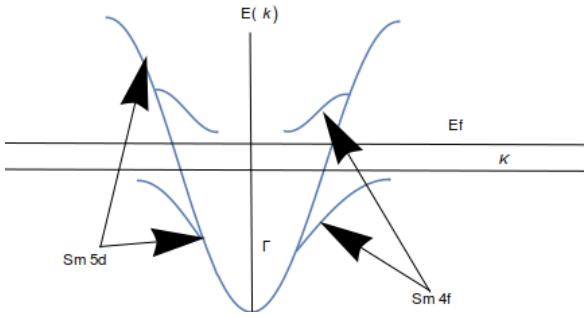

Figure 2.1: The hybridization between localized f-electrons and conduction bands leads to gap opening. The hybridization occurs at the X point, as shown in figure. (After Fig. 2a Ref. [34]).

that Kondo insulators can become topologically ordered due to the large spin-orbital coupling and the hybridization between conduction and f electrons. Despite a long time of experimental and theoretical endeavor, many essential aspects are still under discussion.

2.1.1 Crystal structure

SmB_6 crystallizes in the CsCl type structure (simple cubic structure) with the Sm ions located at the corners and B_6 octahedra located at the body center of the cubic lattice, as shown in Figure 2.2. It has a space group No. 221 ($Pm\bar{3}m$, O_h^1). Its lattice constant is a = 4.133 Å, and the atomic position parameter of boron is $x = 0.199924$ [36].

The bulk Brillouin zone (BZ) of SmB_6 is a cube with six square faces. The center of the cube is the Γ point, while the centers of the square faces are the X points. The lower part of Figure 2.3 shows that each X point and an entirely opposite partner are equivalent, because of the inversion symmetry of the crystal. The Brillouin zone of a [001] is shown above.

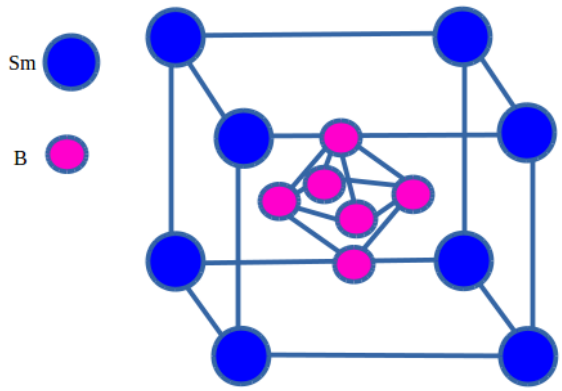

Figure 2.2: The crystal structure of SmB_6 with $Pm\bar{3}m$ space group. The Sm ions are located at the corners and the B_6 octahedron at the center of the cubic lattice.

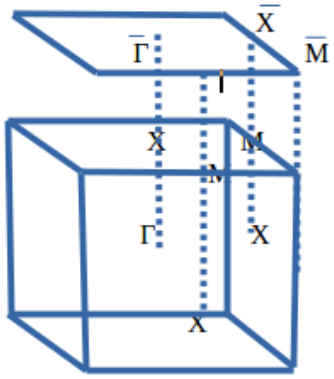

Figure 2.3: The bulk and surface BZs of SmB_6. The Γ-point is at $\vec{k} = (0, 0, 0)$, the X points are at $\vec{k} = \frac{\pi}{a}(1, 0, 0)$ and the M points are at $\vec{k} = \frac{\pi}{a}(1, 1, 0)$ and R point at $\vec{k} = \frac{\pi}{a}(1, 1, 1)$ is not indicated. On the surface BZ, $\bar{\Gamma}$ is at $\vec{k} = (0, 0)$, $\bar{X}$ is at $\vec{k} = \frac{\pi}{a}(1, 0)$ and $\bar{M}$ is at $\vec{k} = \frac{\pi}{a}(1, 1)$.

2.2 SmB_6 electron structure

2.2.1 Electronic configuration

The full form of the Sm electronic configuration is:

$1s^2 2s^2 2p^6 3s^2 3p^6 4s^2 3d^{10} 4p^6 5s^2 4d^{10} 5p^6 4f^6 6s^2$,

in which the Sm^{2+} ion has the same configuration with removal of $6s^2$ electrons:

$1s^2 2s^2 2p^6 3s^2 3p^6 4s^2 3d^{10} 4p^6 5s^2 4d^{10} 5p^6 4f^6$.

While the Sm^{3+} electronic configuration given as:

$1s^2 2s^2 2p^6 3s^2 3p^6 4s^2 3d^{10} 4p^6 5s^2 4d^{10} 5p^6 4f^5$.

Sm $4f$ levels in the presence of SOC (spin orbit coupling) are split first into $J = \frac{5}{2}$ and $J = \frac{7}{2}$ states.

2.2.2 Band calculation of SmB_6

Band structure calculation is a powerful method for investigating electronic structure, in particular the narrow band gap. There are a number of band structure calculations which have done in the past. I am going through some of them to help us understand possible origins of the resistivity plateau for SmB_6.

2.2.2.1 Tight- binding models for samarium hexaboride

The tight-binding model gives a first important step towards a better understanding of the physical properties of SmB_6. The main idea for building a realistic tight binding model for SmB_6 came from a detailed first principle calculations of A. Yanase and H. Harima [37] and of V. N. Antonov et al. [36]. Later on, the calculation of V. N. Antonov, B. N. Harmon and A. N. Yaresko in 2002 [36] for SmB_6 explained the hybridization between $4f$ and $5d$ orbitals. As recently as 2015, C. J. Kang et al. [38], have investigated the band structure and band symmetry of SmB_6.

2.2.2.2 Old calculations

In 1992, A. Yanase and H. Harima calculated the energy band structure of YbB_{12}, SmB_6, and CeNiSn including the spin orbit interaction by using the Linearized Aug-

mented Plane-wave (LAPW) with the local density approximation (LDA) method. According to the results of their calculations, seven bands are well-localized $4f$ bands of Sm. These bands are separated to three and four bands with $J = \frac{5}{2}$ and $J = \frac{7}{2}$ due to the spin-orbit splitting of the $4f$ bands. Further, it was found that a small direct gap between the occupied and unoccupied bands in which the gap is less than 0.001 Ry (0.0136 eV) exists at the Fermi energy along the Δ line in k-space (see Figure 2.4).

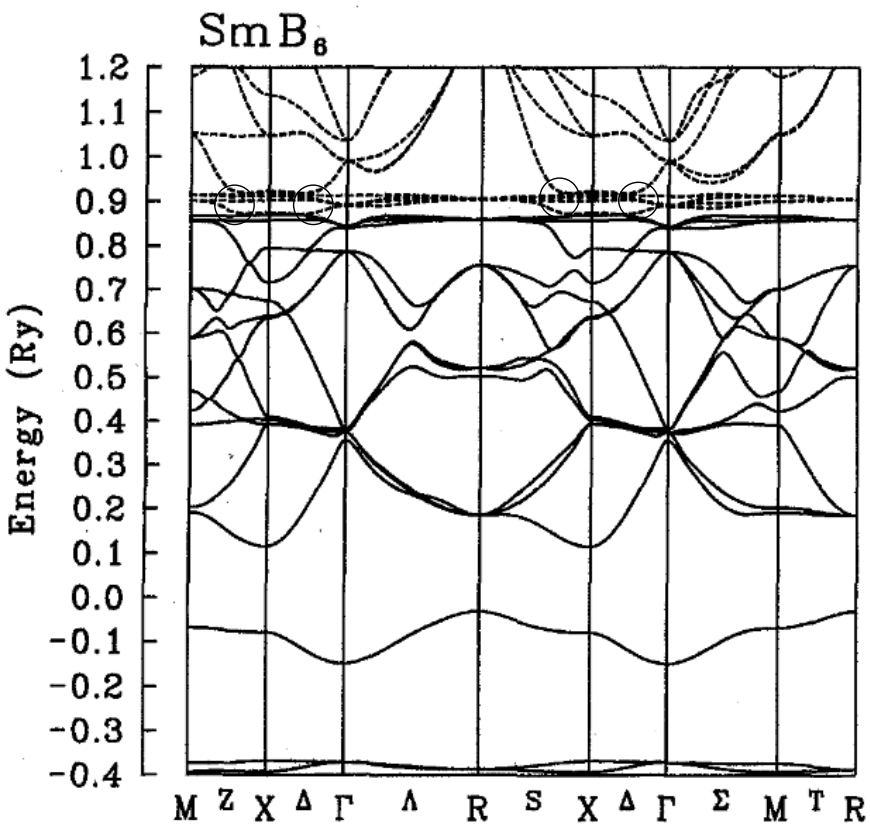

Figure 2.4: Calculated energy band structure of SmB_6 showing the occupied and unoccupied bands. The $4f$ bands with $J = \frac{5}{2}$ appear near 0.86 Ry (11.7 eV) whereas $4f$ bands with $J = \frac{7}{2}$ appear near 0.91 Ry (12.4 eV). Also, two bands are $5p$ bands on Sm with $J = \frac{3}{2}$ near -0.39 Ry (-5.3 eV). The circles indicate where there is hybridization between the $4f$ bands and conduction band. (Reproduced from A. Yanase and H. Harima [37] with permission).

Figure 2.4 shows the hybridization between the $4f$ bands and conduction bands which are located along the Δ, Z and S lines in k-space. Two $4f$ bands in the lower

group hybridize with the conduction band, which consists of bonding orbits between B $2p$ and Sm $5d$ electrons. The places where hybridization are largest is indicated by circles in Fig.2.4.

V. N. Antonov et al. [36] investigated the electronic structure and optical spectra of SmB_6 and YbB_{12}, and calculated energy band structure using the fully relativistic Dirac LMTO band structure method using the LSDA and LSDA+U approximations. This calculation is in good agreement with the previous one by A. Yanase and H. Harima. They found that the energy band structure with the LSDA approximation can be divided into three zones separated by energy gaps. The first zone has mostly B $2s$ character mixed with some amount of Sm sp character (it is not shown because is below the energy range shown in Fig. 2.5). The next group is the B $2p$ bands which are separated from the B $2s$ bands by a gap of 3 eV. The flat Sm $4f$ bands are near the Fermi energy. The Sm $5d$ bands are partly occupied, and they are also separated from B $2p$ states by the energy gap around 0.7 eV at the X-point as seen in the Figure. 2.5. Thus, at Fermi level, there is a small direct energy gap about 23 meV.

I should also mention that the measurement of the optical conductivity spectrum in Ref. [36] contains key features of both divalent Sm^{2+} and trivalent Sm^{3+}, consistent with the mixed valence character of SmB_6 seen in the band structure calculations.

2.2.2.3 New calculations

Recently, Feng Lu et al. [42] proposed that SmB_6 is a strongly correlated topological insulator with unique surface states containing three Dirac cones on the (001) surface. Dirac cones are surfaces that describe the electronic energy dispersion; $\epsilon(k) \sim k$, i. e. the dispersion is linear with k; they can be directly detected by angle-resolved photoemission spectroscopy (ARPES). They have employed the local density approximation

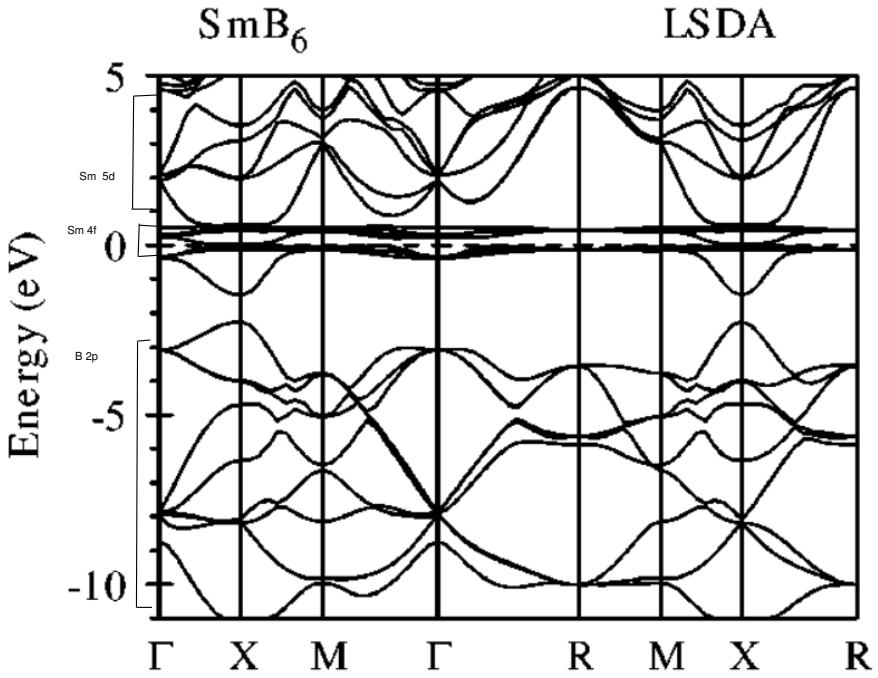

Figure 2.5: Self consistent fully relativistic, spin polarized energy band structure and total DOS calculated for SmB_6 with the LSDA and LSDA+U approximations. (Reproduced from V. N. Antonov et al. [36] with permission)

with Gutzwiller method combining with a Green's function scheme to study SmB_6. Consequently, their results and the dynamical mean-field theory (DMFT) method show that the separation between $4f$ electron bands is much larger than what was previously found using density functional theory (DFT). That is because DFT cannot capture the strong correlation of $4f$ electron bands. As a result, they have concluded that the DFT method gives unphysical results because the overlap between the $J = \frac{5}{2}$ and $J = \frac{7}{2}$ bands that lead the band and the corresponding wave functions at the Γ and X points to have the wrong symmetry and shape.

Later, C.-J. Kang et al. [38] have investigated the band structure of SmB_6 using density functional theory (DFT). Moreover, they included the strong correlation effect by a 10 times enhanced spin-orbit coupling (SOC) for Sm $4f$ electrons. Additionally, they applied the full-potential linearized augmented plane wave (FLAPW)

band method and projector augmented wave (PAW) band method.

Their complete results show the 0.018 eV band gap and Sm $4f$ bands are dominant near E_F, where $J = \frac{5}{2}$ states are located below E_F and $J = \frac{7}{2}$ states are above E_F with about 1 eV energy split between these states. In order to have separation between $J = \frac{5}{2}$ and $J = \frac{7}{2}$ bands similar to that from DMFT, they used DFT and 10 times enhanced spin orbit coupling, which removes unphysical overlap between $J = \frac{5}{2}$ and $J = \frac{7}{2}$ bands without modifying the orbital characters significantly. As a result, the $J = \frac{5}{2}$ and $J = \frac{7}{2}$ bands are well separated with about 6 eV and the band overlap between them is reduced. Although this method makes the Sm-d and B-p bands shifted slightly up, the band gap is increased from 18meV to 43 meV and the band structure is still identical.

In summary, the size of the energy gap varies considerably with different methods that used to calculate the band structure. The LAPW with LDA method [37] shows the gap is less than 13.6 meV. Fully relativistic Dirac LMTO band structure method [36] gives a result of 23 meV, and the density functional theory (DFT) [38] shows that the band gap is 43 meV. All of these results are large than the activation gap observed in resistance measurements.

Chapter 3

Quantum Oscillations

The de Haas–van Alphen effect is a quantum mechanical effect in which the magnetisation and other measurements of a metallic crystal oscillate as a function of the inverse applied magnetic field. It is a powerful technique for measuring the Fermi surface, as since the oscillation frequency depends on the external area of the Fermi surface perpendicular to B. In this chapter, I used the published data of dHvA experiments to fit it for 3D and 2D Fermi surfaces of SmB_6 .

3.1 De Haas-van Alphen effect

The electrons in any system are characterized by their quantum number $\vec{k} = \frac{2\pi}{L}(n_x, n_y, n_z)$ and the energy of free electrons is given by:

$$E(k) = \frac{\hbar^2 k^2}{2m} \tag{3.1}$$

In 2D, without magnetic field, electrons in the sample are allowed to occupy any of the quantum states in momentum space that lie within the Fermi disk $E(k) \leq E_F$ as shown in Figure 3.1(a). However, in the magnetic field B the Lorentz force influences

the electrons to take a circular motion.

The Hamiltonian of an electron in a magnetic field is:

$$H = \left(\frac{\vec{p} - q\vec{A}(\vec{r}, t)}{2m} \right)^2 + qV(\vec{r}) \tag{3.2}$$

where q is electric charge, $V(\vec{r})$ is a scalar potential, and $\vec{\nabla} \times \vec{A} = \vec{B}$ is a vector potential, when $\vec{B}$ points perpendicular to the sample. We can rewrite the Hamiltonian with the theory of harmonic oscillators as:

$$H = \hbar w_c \left(n + \frac{1}{2} \right) \tag{3.3}$$

where $w_c = \dfrac{eB}{mc}$, and n is an integer. Hence the energy levels of the 2D system are:

$$E_n = (n + \frac{1}{2})\hbar w_c. \tag{3.4}$$

There energy levels can be drawn in k-space as:

$$\frac{\hbar \left(k_x^2 + k_y^2 \right)}{2m} = \left(n + \frac{1}{2} \right) \hbar w_c \tag{3.5}$$

as shown in Fig 3.1.

In the 3D system, if the field points in the z-direction, the eigenvalues of the Hamiltonian are determined by the quantum numbers k_z, and n,

$$E_{k_z,n} = \frac{\hbar^2 k_z^2}{2m} + (n + \frac{1}{2})\hbar w_c, \tag{3.6}$$

where n is a non-negative integer.

Hence the moments in the plane perpendicular to B is quantised, which is known as Landau quantization. The electrons are restricted to the cylinders in k space

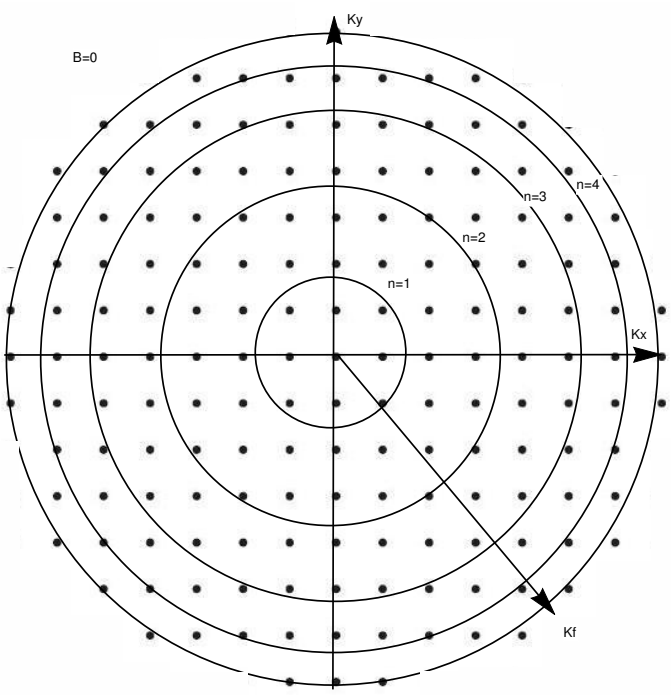

Figure 3.1: Electron states in the k space 2D system. When $B = 0$ there is one state per area $(\frac{2\pi}{L})^2$. While at $B \neq 0$, the electron energy is quantized into Landau levels and each circle has energy $E_n = (n + \frac{1}{2})\hbar w_c$.

defined by $\frac{\hbar\left(k_x^2+k_y^2\right)}{2m} = \left(n + \frac{1}{2}\right)\hbar w_c$, as shown in Figure 3.2; these cylinders are known as"Landau tubes", which shrink as B is increased.

As the magnetic field is increased, the space between Landau tubes increases and the number of tubes inside the Fermi sphere decreases as the tube passes through the Fermi surface. In general, when any Landau tube crosses an extremal orbit, as shown in Figure 3.3, the metal's properties will oscillate as a function of $\frac{1}{B}$. The oscillation frequency is given by:

$$F = \frac{\hbar c}{2\pi e} A, \tag{3.7}$$

where $\dfrac{hc}{e} \equiv \phi = 4.14 \times 10^{-11}$ T cm^2 is the flux quantum, and A is the cross sectional area of the Fermi surface in k space. Note that the frequency will has units of Tesla. This oscillation is known as a magnetic quantum oscillation. Quantum oscillations ap-

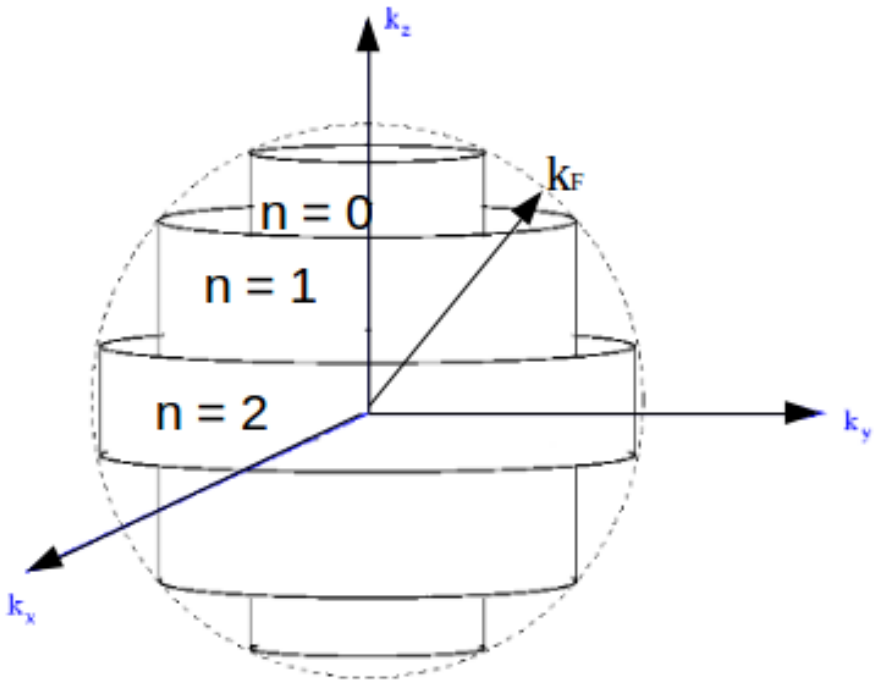

Figure 3.2: In 3D system with magnetic field, the electrons are restricted to the cylinders within the Fermi-sphere.

pear in many measurements, however, we are interested to study only the oscillations of the magnetization, which is known as the de Haas-van Alphen (dHvA) effect. The dHvA effect is a powerful technique discovered by de Haas and van Alphen in 1930 [52] for measuring the Fermi surface. This technique is applied at low temperatures and strong magnetic field, and it provides details of the extremal areas of a Fermi surface. De Haas-van Alphen oscillations are a thermodynamic effect, as a result from the Landau quantization of the electronic spectrum. By changing the magnetic field direction, different cross-sectional areas of the Fermi surface can be mapped out. In this way, the whole Fermi surface can be mapped. The period of oscillation is found by the Fourier transformation of magnetisation oscillations.

In 2D, when the strength of the field B increases, the radius of the circular orbits will increase until an orbit "pops out" of the Fermi surface. This leads to oscillatory

behaviour in the magnetization and the free energy. As the orbits pass through the Fermi surface, they instantaneously become un-occupied, and the oscillations in the free energy will have a maximum amplitude. However, in a 3D system (Fig 3.3), the circles are replaced by cylinders. As B increases, the radius of the cylinders increases and the cylinders emerge continuously without dramatic change from the Fermi sphere as the radius of the cylinder passes this extremal radius. As a result, the magnetisation in 3D oscillation are not as sharp (singular) as the 2D case.

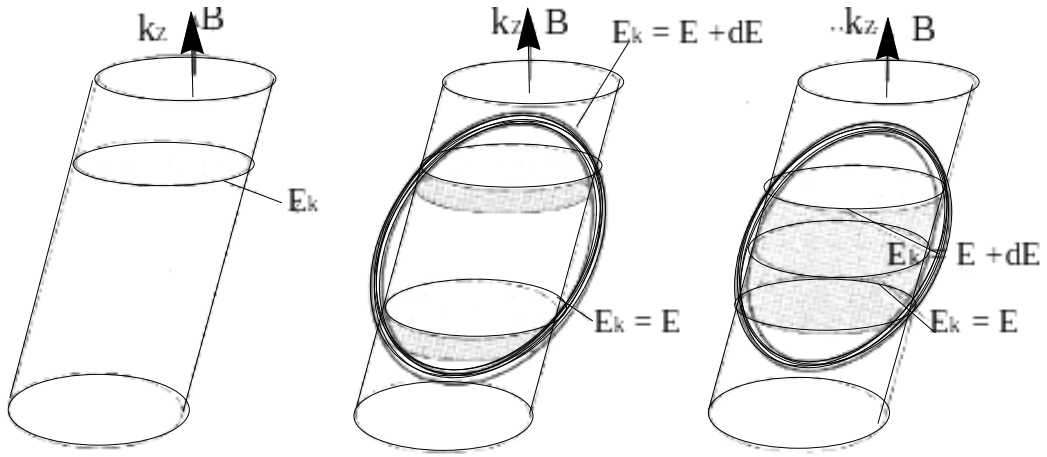

Figure 3.3: (a) Landau tube is containing the electrons orbits in the n^{th} Landau level with energy equal to the Fermi energy of the sample. (b) There are small amount of the electrons which are at the intersection area between the Landau tube and the Fermi surface can remain in the states. (c) The Landau tube is tangent to a Fermi surfaces and the intersection is extremal orbit which is always perpendicular to the applied field.

3.1.1 Technique for the measurement of dHvA

To measure the de Haas-van Alphen oscillations, there are two major techniques. The first is the field modulation method and the second is the torque method. In this work, we are interested in examining experiments which use the torque method.

3.1.1.1 Field modulation method

This method can be used to study the behavior of $\vec{M}$. The system consists of three coils: detecting, compensation, and field modulation coils; each coil has an important role. The field modulation coil generates an alternating magnetic field which produced electromotive forces in both detecting and compensation coils. Then, the alternating voltage is induced in the detecting coil. This voltage contains a component proportional to $\frac{\partial M}{\partial B}$, where M is the magnetisation of the sample. The signals obtained from detecting coil are periodic in $\frac{1}{B}$. The Fourier analysis of the collected data can obtain the dHvA frequency Eq.(3.7).

3.1.1.2 Torque method

The torque measures the absolute value of the magnetization. The magnetic torque $\vec{\tau} = V\vec{M} \times \vec{B}$ acts on the sample when an external magnetic field is applied to the sample and is $M_{\perp}BV$, where V is the volume, B is the external magnetic field applied to the sample and $M_{\perp}$ is the component of $\vec{M}$ perpendicular to $\vec{B}$.

3.2 Using de Haas-van Alphen to measure the Fermi surface of SmB_6

There have been two dHvA studies of SmB_6 with differing conclusions: one determined the Fermi surface to be 2D, and the other to be 3D. In this section, we will discuss these results.

3.2.1 Samarium hexaboride with 2D Fermi surface

In this section, we discuss the data of [45]. In their work, the torque magnetometer method was used. The SmB_6 single crystal samples used were grown by the flux method and then each one was etched with acid to remove the residual aluminum flux. Their measurements were performed at 0.3 K with the magnetic field up to 45 T across a range of tilt angles.The tilt angle ϕ is the angle between the applied field and one of the main cubic axes of the crystal. Magnetisation oscillations were measured for each tilt angle and were each analyzed using a fast Fourier transform. Three Fourier transform peaks were observed, corresponding to three different Fermi surfaces labelled as α, β, γ and shown separately in Figs. 3.4, 3.5, 3.6. Also, the results show that the Fermi surfaces appear to be two-dimensional (2D) and arise from the crystalline (101) and (100) surfaces. To understand the idea of different surfaces, I am going to explain each one of them as described in Ref. [45].

3.2.1.1 α, β, and γ surfaces

The first oscillation frequency F^{α} was observed at frequency 30.5 T. This is attributed to the (100) surface families. Three branches of F^{α} are observed, because of the fourfold symmetry of the SmB_6 cubic structure, with minima at $\phi_0 = 0°$, and 90°. The data are fit to $F_0/|\cos(\phi - \phi_0)|$, which corresponds to a cylindrical fermi surface aligned in the (100)directions associated with each of the (100) surfaces of the crystal, as shown in Figure 3.4.

Second, the oscillation frequency F^{β} observed at frequencies higher than 900 T, shown in Fig. 3.5. It shows a large angular dispersion and tracks the 2D angular dependence associated with (101) surface families. Due to the fourfold crystalline symmetry, several branches are observed within minima at $\phi = -45^o$, and 45°. The data are fit to the functions $F_0^{\beta}/|\cos(\phi + 45°)|$, and $F_0^{\beta}/|\cos(\phi - 45°)|$ corresponding

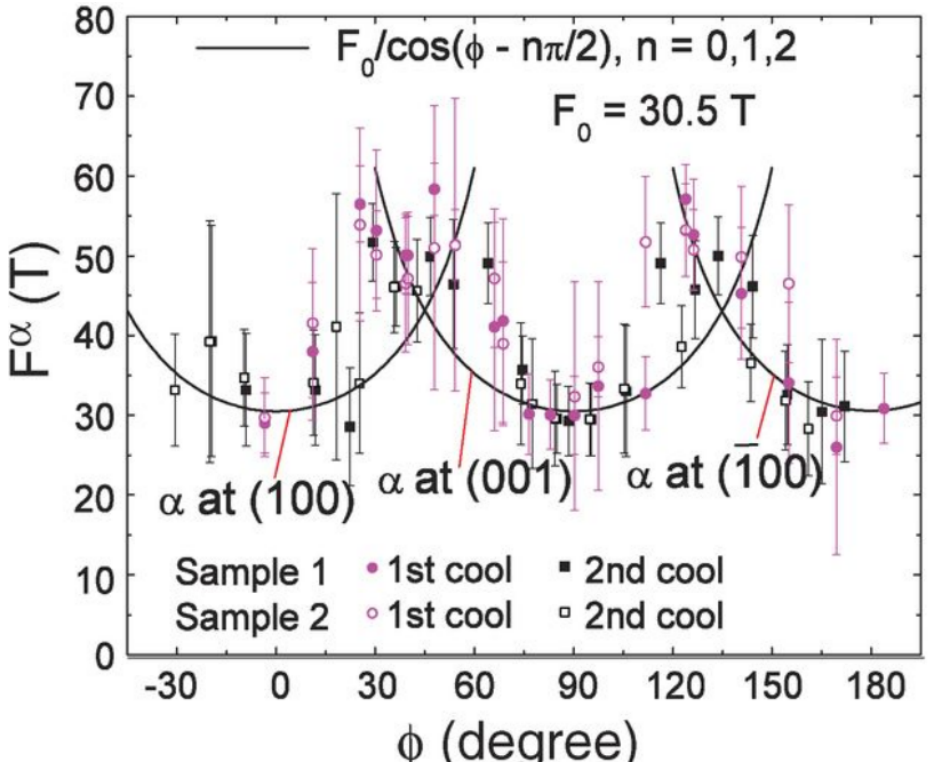

Figure 3.4: The oscillating frequency F^{α} in SmB_6 of the observed Fermi surfaces α is shown as a function of ϕ. Solid lines are fits to $F_0/|\cos(\phi - \phi_0)|$ (a 2D Fermi surface) with $\phi_0 = 0°$, and 90°. (Reproduced from G. Li, et al. [45]).

to cylindricals fermi surface aligned in the (101)directions associated with each of the (101) surfaces of the crystal.

Similar to F^{α}, Fig. 3.6 shows the angular dependence of the oscillating frequency F^{γ} that is observed at 385 T. The γ pockets arise from Fermi cylinders on the (100), (001), and $(\bar{1}00)$ surfaces and the F^{γ} pattern has fourfold crystal symmetry. There are three branches located around $\phi = 0°$, and 90°. The angular dependence is fit by the functions $F_0^{\gamma}/|\cos(\phi - 0°)|$, $F_0^{\gamma}/|\cos(\phi - 90°)|$, and $F_0^{\gamma}/|\cos(\phi - 180°)|$.

To summarize, G. Li, et al. [45] measurements used a magnetic field up to 45 T and temperature down to 0.03 K. They observed a small ellipsoidal Fermi surface (low frequency) which they associate with surface states, and conclude that SmB_6 has 2D topological surface states.

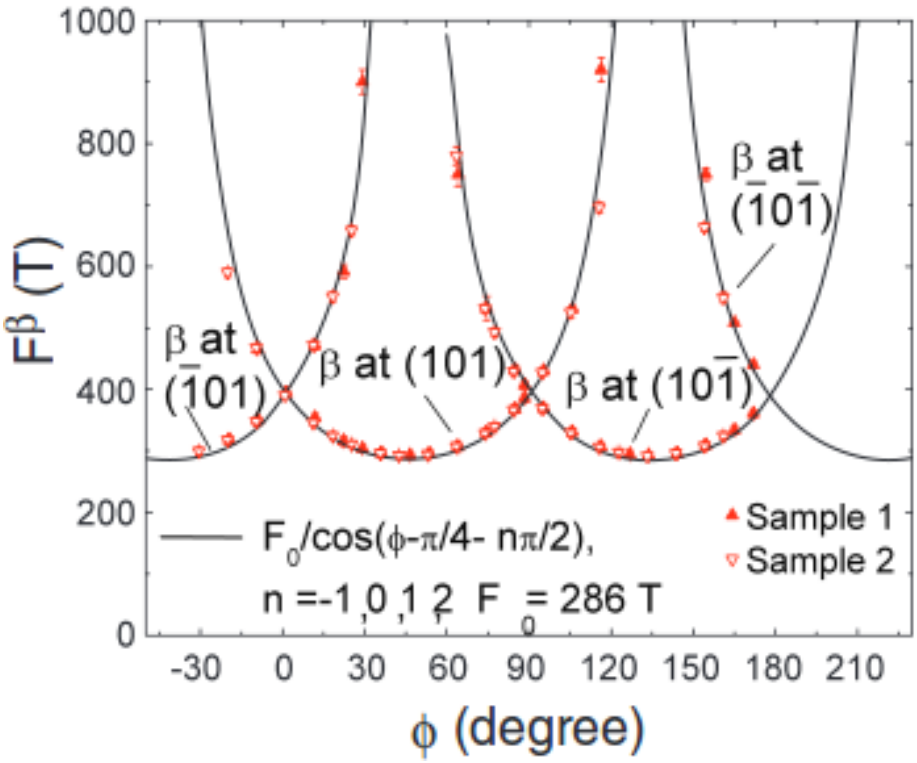

Figure 3.5: The oscillating frequency F^{β} of SmB_6 is shown as a function of ϕ. The solid lines are fits to $F_0/|\cos(\phi - \phi_0)|$ (a 2D Fermi surface) with ϕ_0 = -45°, and 45°. (Reproduced from G. Li, et al. [45]).

3.2.2 Samarium hexaboride with 3D Fermi surface

On the other hand, B. S. Tan et al. [44] observed a large three-dimensional Fermi surface similar to PrB_6 and LaB_6 (metallic rare earth hexaborides), centered at X point of Brillouin zone. They have used both high and low frequency oscillations. Their results were six Brillouin zone (BZ) X-point ellipsoids that are large enough to overlap. This overlap generates "necks" on the Fermi surface. The high-frequency oscillations, which were bigger than 1 kT, helped to observe a 3D Fermi surface occupying half the BZ, while the lower ones helped to discover small orbits located at the necks between the large Fermi surface shapes.

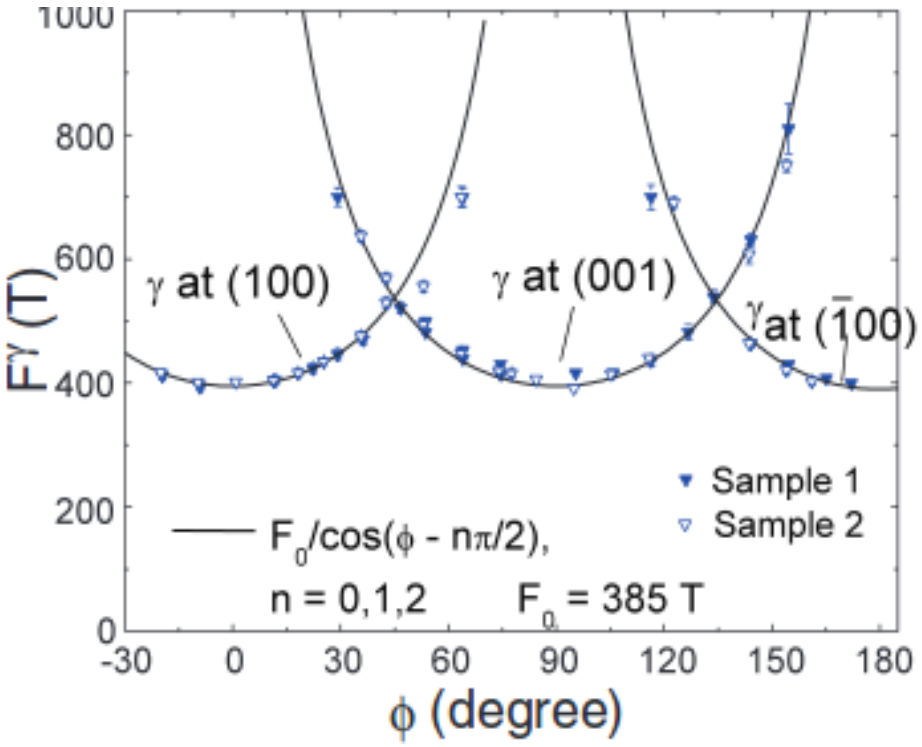

Figure 3.6: The oscillating frequency F^{γ} in SmB_6 is shown as a function of ϕ. The solid lines are fits to $F_0/|\cos(\phi - \phi_0)|$ (a 2D Fermi surface) with $\phi_0 = 0°$ and $90°$. (Reproduced from G. Li, et al. [45]).

3.3 Fermi surface shape in SmB_6: 3D and 2D fits

In this section, I will investigate Fermi surface shape determined by magnetisation oscillation to see if they are better described by 2D or 3D Fermi surfaces. I use the data from G. Li, et al. [45], to fit 3D surfaces for each of the α, β, and γ oscillations. The relation between the extremal area A in k-space and the dHvA frequency$F$ (given in units of Tesla) is

$$A = 2\pi \frac{e}{\hbar c} F \tag{3.8}$$

$$= 9.53585 \times 10^{11} \times F \mathrm{cm}^{-2} \tag{3.9}$$

The cross-sectional area of an ellipse takes the form

$$A = \frac{a^2 c\pi}{\sqrt{a^2 \sin^2\theta + c^2 \cos^2\theta}}, \tag{3.10}$$

where a and c are the lengths of the semi-principal axes, and θ is the angle of the cross section. When $c \gg a$, the Fermi surface shape becomes cylindrical, i.e. 2D, and the cross sectional area is

$$A = \frac{a^2\pi}{|\cos\theta|} \tag{3.11}$$

First, I fit the data to Eqs. 3.10 and 3.11 to find the shapes of Fermi surfaces of the α , β, and γ surfaces separately. These results are summarized in Table 3.1 .To compare these results (2D, and 3D fit) we will need to know χ^2,

$$\chi^2 = \sum_i \frac{(x_i - d_i)^2}{\sigma_i^2} \tag{3.12}$$

where d_i is the measured dHvA frequency, x_i is the frequency given by the best fit model, and σ_i is the error bar for each data point. Then we need to find $\frac{\chi^2}{N}$ which should be approximately 1, where N is the number of points in the dataset.

The χ^2 values are significantly reduced between the 2D and 3D fits for the α and γ oscillations. In these cases, the fitted values a and c (3D case) are within a factor 3, which suggested that 3D ellipsoid model describes the data better than the 2D cylinder model. However, the β fits are not significantly improved when the extra parameter c is included which suggests that the 3D model is not better than the 2D model; moreover the large value for $\frac{\chi^2}{N}$ suggests that neither model is very good. Only for the γ oscillations we find $\frac{\chi^2}{N} \sim 1$ which indicates that the 3D fit is consistent with the experimental data and uncertainties.

Figures 3.7-3.9 shows the angular dependence of the dHvA frequency for each

	3D fit (ellipsoid)			2D fit (cylinder)		
Surface	a (cm^{-1})	c (cm^{-1})	$\frac{\chi^2}{N}$	a (cm^{-1})	$\frac{\chi^2}{N}$	N
α	$2.30 \pm 0.02 \times 10^6$	$4.9 \pm 0.7 \times 10^6$	0.35	3.14 ± 0.04	0.65	74
β	$6.61 \pm 0.06 \times 10^6$	$42 \pm 9 \times 10^6$	5.5	9.39 ± 0.07	6.3	66
γ	$7.78 \pm 0.04 \times 10^6$	$26 \pm 18 \times 10^6$	1.5	10.97 ± 0.07	4.62	50

Table 3.1: Table of the results of fits the data to Eqs. 3.10 and 3.11.

of the α, β, and γ surfaces. These come from fitting the data set from Ref. [45] to the 3D model. The results of the fit to the 2D model produces figures that are indistinguishable from the 3D model.

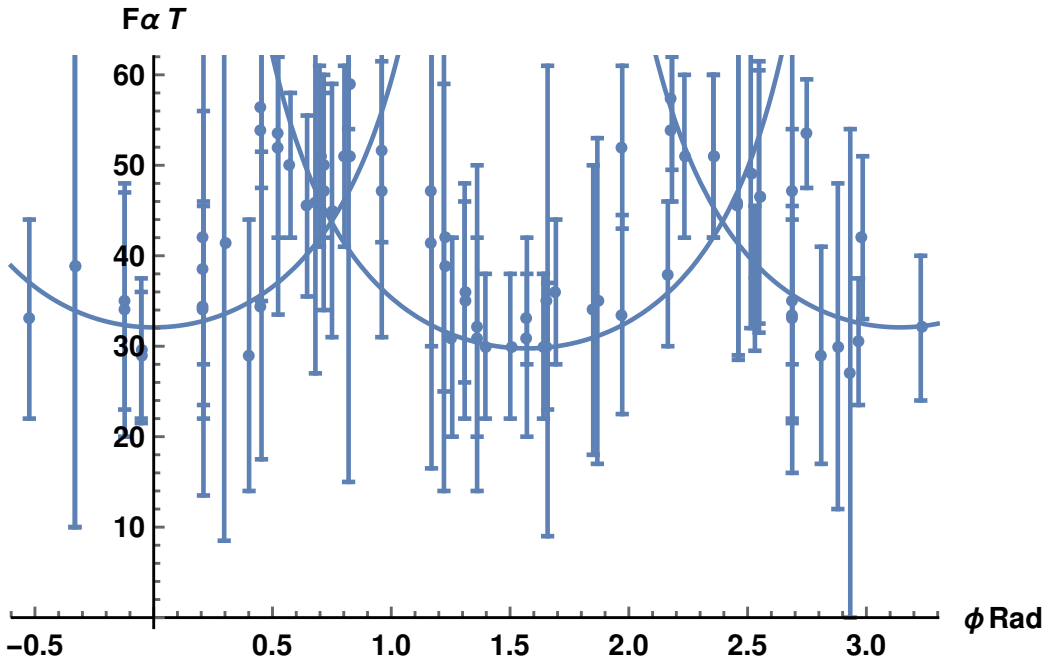

Figure 3.7: Angular dependence of the dHvA frequency F^{α}. The solid lines are our fit to 3D equation, and the dots are the data extracted from the Fig. 3 A in Ref. [45].

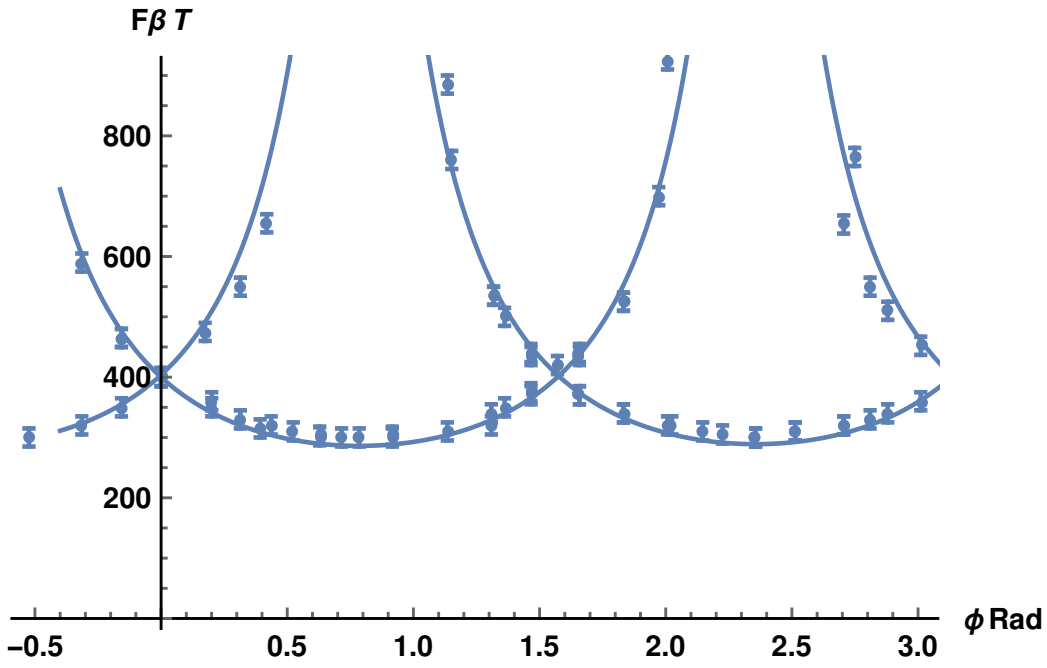

Figure 3.8: Angular dependence of the dHvA frequency F^{β}. The solid lines are our fit to 3D equation, and the dots are the data extracted from the Fig. 3 B in Ref. [45].

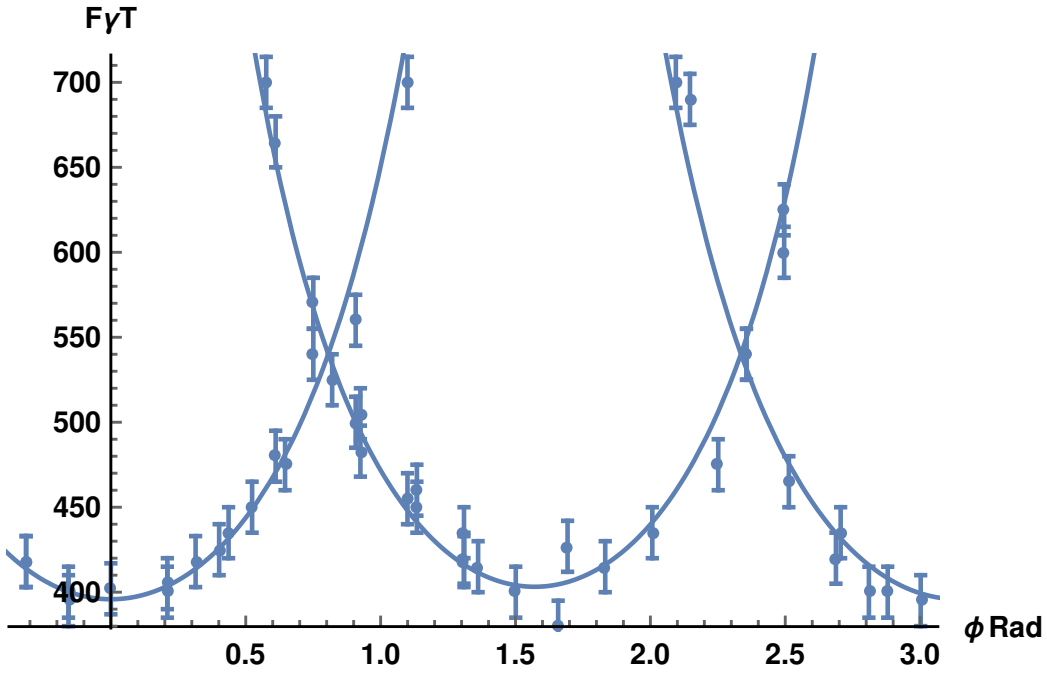

Figure 3.9: Angular dependence of the dHvA frequency F^{γ}. The solid lines are our fit to 3D equation, and the dots are the data extracted from the Fig. 3 C in Ref. [45].

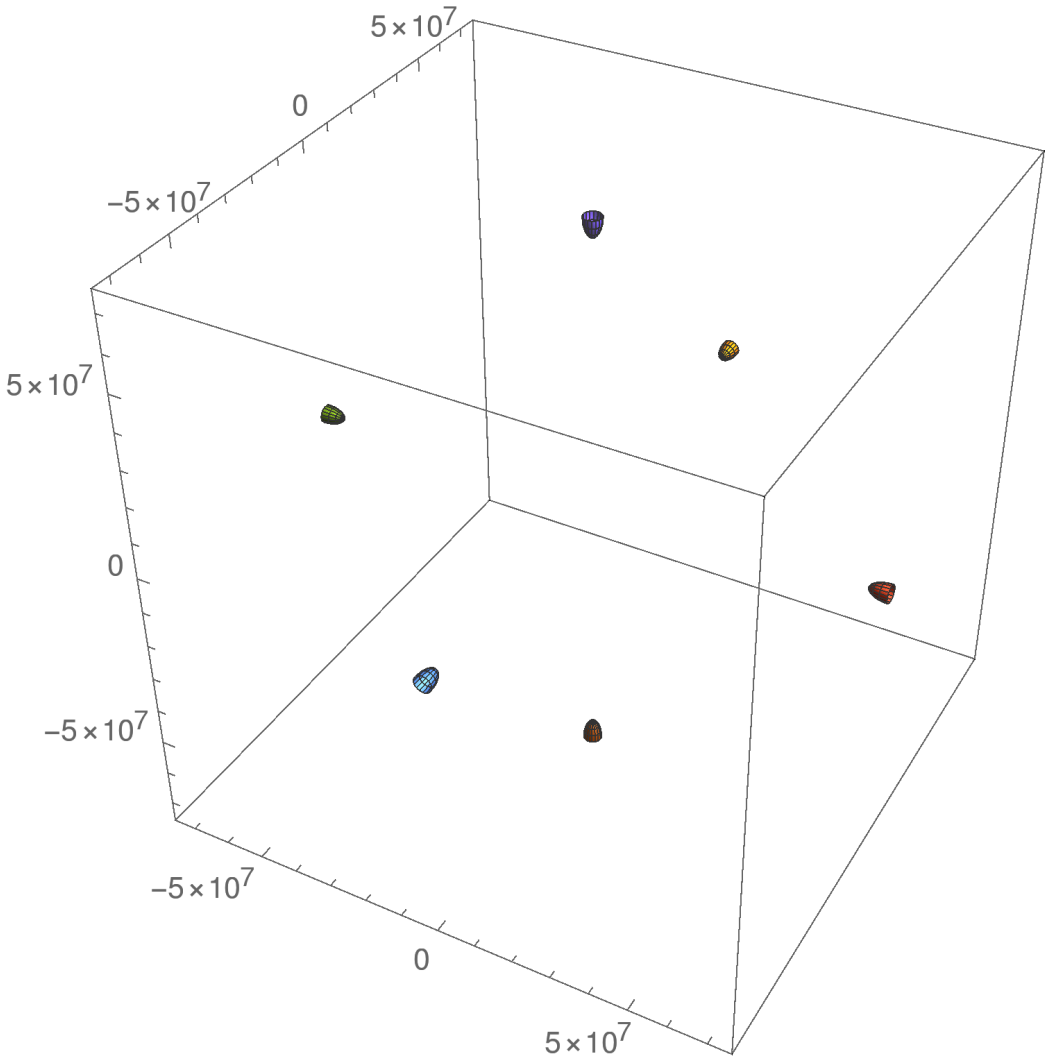

Figure 3.10: Fermi surfaces of the α surface, drawn using the results of our 3D fit.

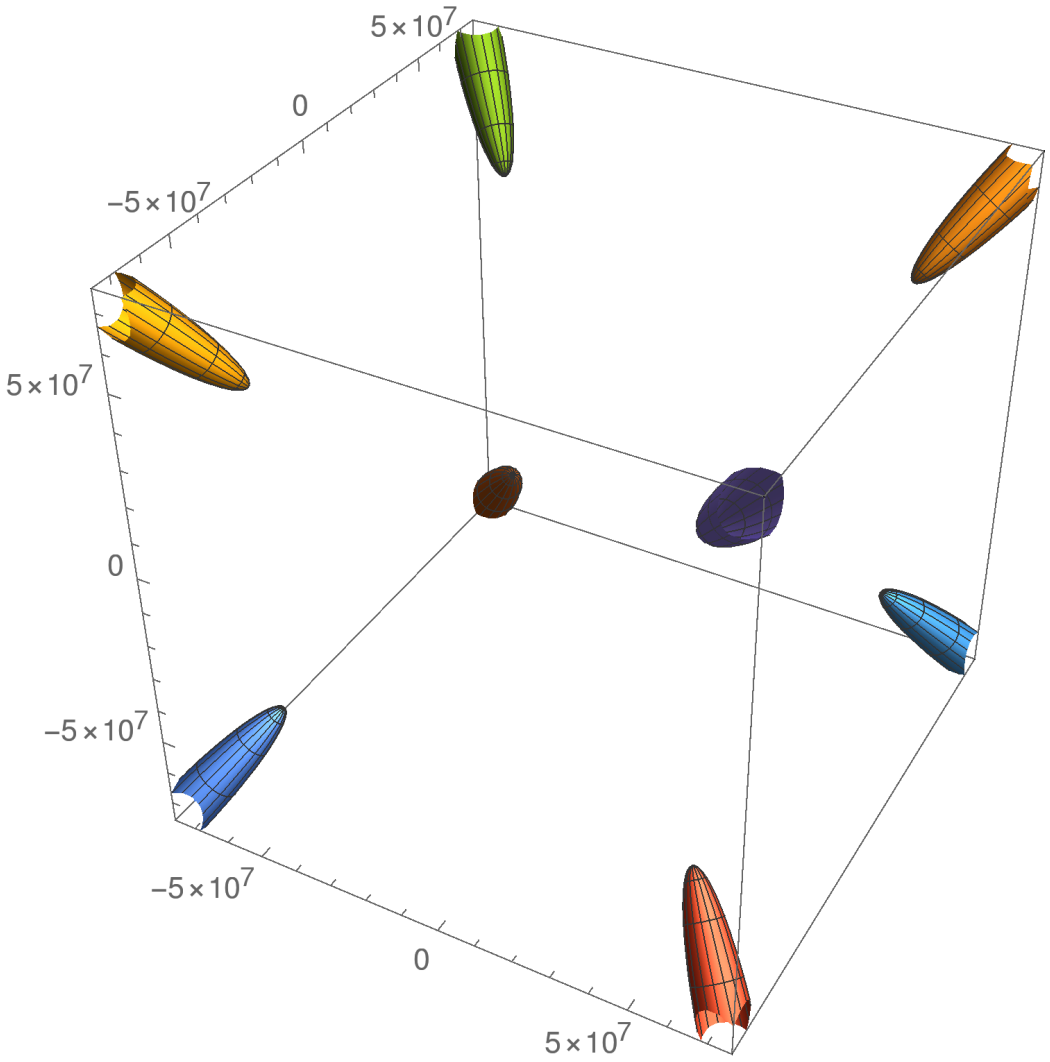

Figure 3.11: Fermi surfaces of the β surface, drawn using the results of our 3D fit.

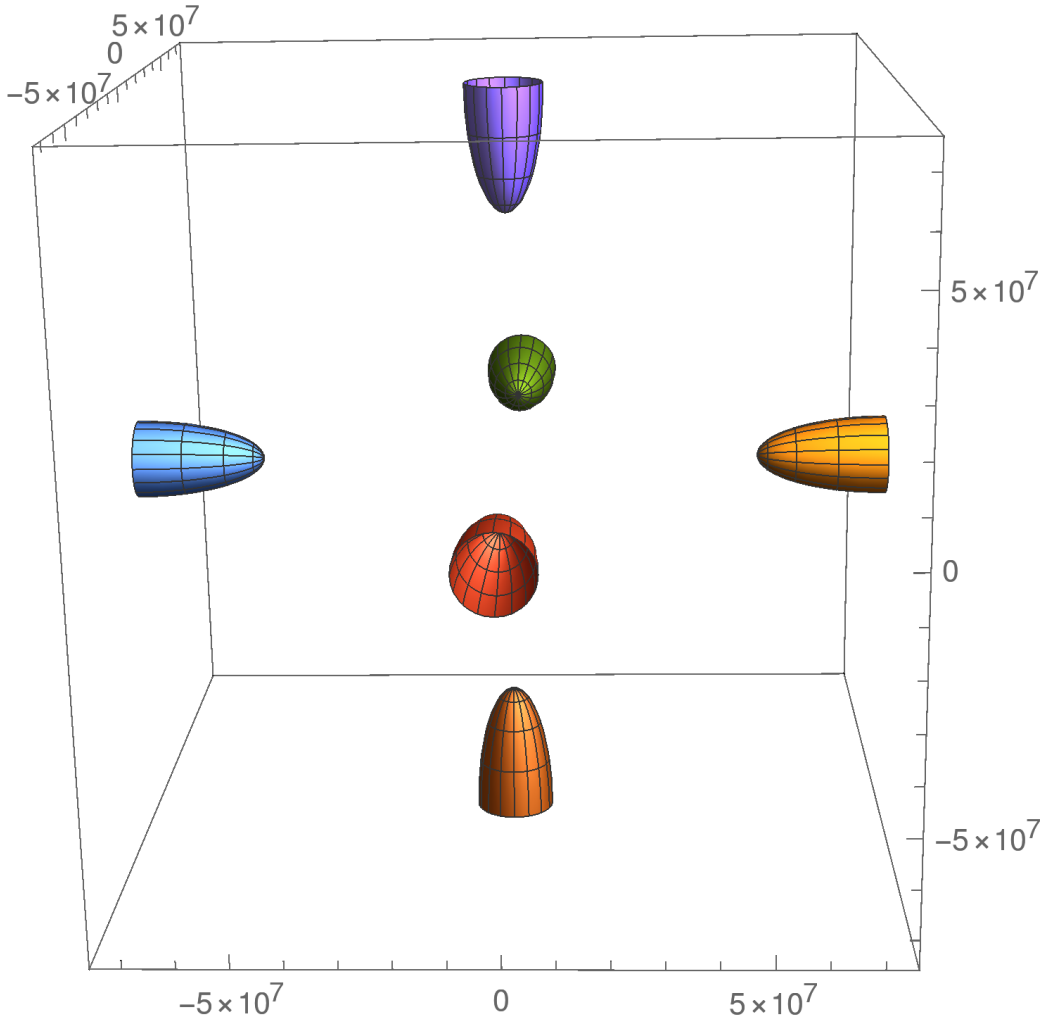

Figure 3.12: Fermi surfaces of the γ surface, drawn using the results of our 3D fit.

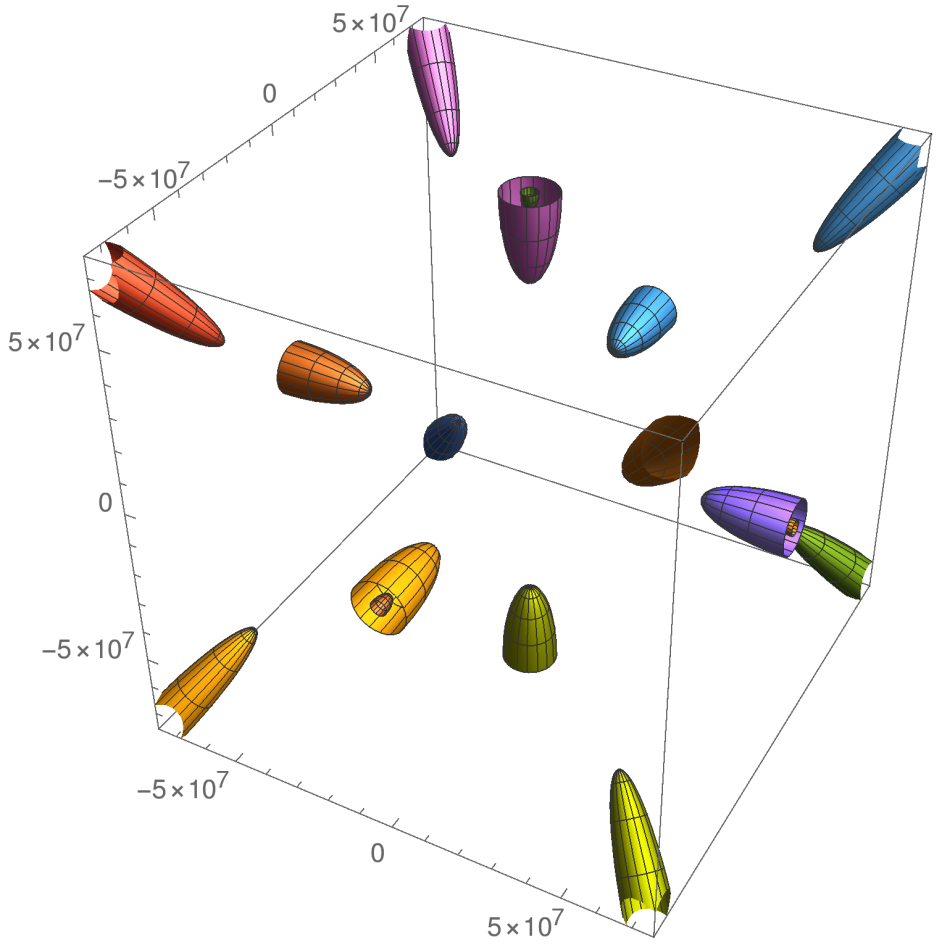

Figure 3.13: The shape of SmB_6 Fermi surfaces 3D fit according to the results of the 3D fits. This figure shows the results of Figs. 3.10, 3.11, and 3.12 all together.

Figure 3.13 shows the shape of SmB_6 Fermi surfaces where the elongated β surfaces located at the corners and γ surfaces located at the faces while the 3D α surfaces located inside the γ surfaces.

To conclude, we find that the β surface is compatible with a 2D Fermi surface, or of 3D Fermi surfaces that are elongated ellipsoids as Ref [45] showed. On the other hand, the χ^2 values and the values of a and c in the 3D fits for the α and γ surfaces indicate the Fermi surfaces associated with the α and γ branches have 3D ellipsoidal shapes.

Chapter 4

Resistivity of SmB_6

4.1 Resistivity of SmB_6

Despite the fact that the SmB_6 has long been known as a Kondo insulator [**?**,21,30,33], with strong correlations and band hybridization (see Chapter 2), some of its essential properties still defy understanding. One of these mysteries is electrical conductivity of SmB_6 at very low temperature, and what is responsible for this low-temperature behavior.

The resistivity of SmB_6 and the magnitude of its Hall coefficient increase dramatically with decreasing the temperature, while the most remarkable phenomenon is seen at temperatures lower than 4 K, where the resistivity and Hall do not continue to rise, but instead they saturate and remain finite as $T \to 0$. In other words, SmB_6 behaves electronically at high temperatures like a semiconductor, and at low temperature, its resistance mysteriously saturates [63].

S. Wolgast et al. [55] studied the transport of SmB_6 with a specialized sample geometry to study the mystery of the residual resistivity. As a result, their experiments seems to indicate that as the temperature is reduced, SmB_6 goes from a 3D bulk

conductor to a 2D surface conductor with an insulating bulk. In order to determine whether the conduction is dominated by surface or bulk, they used a thin sample of SmB_6 with eight coplanar electrical contacts, (four on each side of the sample) as shown in Figure 4.1.

In the conventional lateral measurement R_{lat} (Figure 4.1(a, b)) the contacts are only on one side. This arrangement cannot tell whether the conduction at low temperature is bulk dominated or surface dominated. At high temperature, all the current will flow on the front side contact. But at low temperature, where the resistivity becomes large, the current will still flow on the front side for both cases (bulk or surface dominated). It is easy to notice that R_{lat} is very similar in both cases, and this explains why R_{lat} alone can not distinguish whether the conduction is bulk dominated or surface dominated.

Likewise, a hybrid measurement R_{hyb} is made by passing current through two front side contacts, but the voltage is across two back side contacts (see Figure 4.1(e, f)). At high temperature R_{hyb} should be identical to R_{lat} in both cases (bulk or surface conductor). At low temperature if the bulk remains conducting, the current will still follow as same as R_{lat} case. However, if the surface remains conducting, the front side will have most the current and a tiny current will flow around the back side. Then R_{lat} will be much larger than R_{hyb}.

However, in the vertical contact configuration R_{vert} the current passes from one front side contact to the back side contact with the voltage applied between the front side and back side contact (see Figure 4.1(c, d)). At high temperature, if the bulk is conductive, all the current flows perpendicularly through the sample. Due to the large distance between the voltage contact and the current contact, there is no current near the voltage contacts and R_{vert} will be very small. At low temperatures where the resistivity increases significantly, the current will continue to flow as long as the

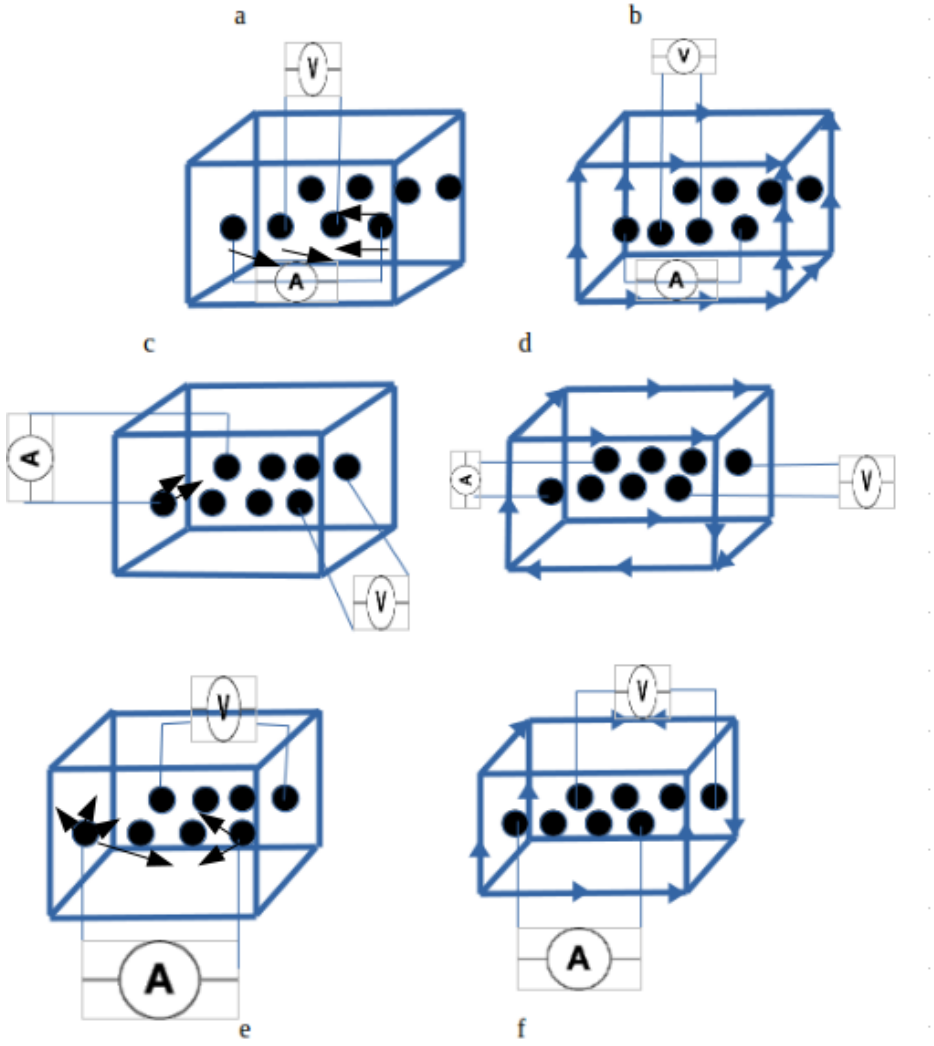

Figure 4.1: Different configurations of electrical contacts. Arrows indicate current direction. The figures on the left hand side show the cases when the bulk is conductivity, and the right hand side figures show the cases of an insulating bulk. (a) lateral measurement R_{lat} where the current passes through the bulk. (b) R_{lat} configuration where the bulk becomes insulating and the current flows around the surface. (c) R_{vert} configuration, where the current passes horizentally through the bulk. (d) R_{vert} where the bulk becomes insulating and the current forced to flow around the surface. (e) Hybrid measurement R_{hyb} for conducting bulk. (f) R_{hyb} for insulating bulk. (Based on Ref. [55], Fig 3).

bulk is conductive. However, if the surface is conductive, the entire current will be forced to flow around the surface of the sample and the R_{vert} will be very large.

In all cases, if the surface conductivity is the same as the bulk conductivity, for all three measurement configurations the resistance will be proportional to the resistivity with a proportionality constant $R = C\rho$ that depends on the geometry of the sample. For example, in the textbook case of long, thin wire $C = \frac{L}{A}$, where L is the length and A is the cross-section area. However, if the surface has a high conductivity, there is no simple dependence of resistance on geometry or temperature.

In order to examine the resistivity and the conductivity of SmB_6, we are going to study two different cases.

4.1.1 Bulk conductor (non-topological insulator)

The conductivity in this case depends only on the temperature and the sample geometry,

$$\sigma \propto \exp^{\frac{-E_g}{K_B T}} . \tag{4.1}$$

Experiments show that the conductivity can be described by

$$\sigma = \sigma_a + \sigma_b \exp^{\frac{-E_g}{K_B T}} . \tag{4.2}$$

The second term is the conductivity of semiconductor, with gap E_g. The first term is a temperature independent constant, which can interpreted as a bulk feature associated with hopping of some kind. The resistivity also depends on the temperature $\rho = \dfrac{1}{\sigma}$,

$$\rho = \frac{1}{\sigma_a + \sigma_b \exp^{\frac{-E_g}{K_B T}}}. \tag{4.3}$$

The resistance R will be proportional to the resistivity,

$$R = \frac{C}{\sigma_a + \sigma_b \exp^{\frac{-E_g}{K_B T}}}. \tag{4.4}$$

Figure 4.2 shows the temperature dependence of the electrical resistivity and conductivity based on Eq. 4.2 and Eq. 4.3.

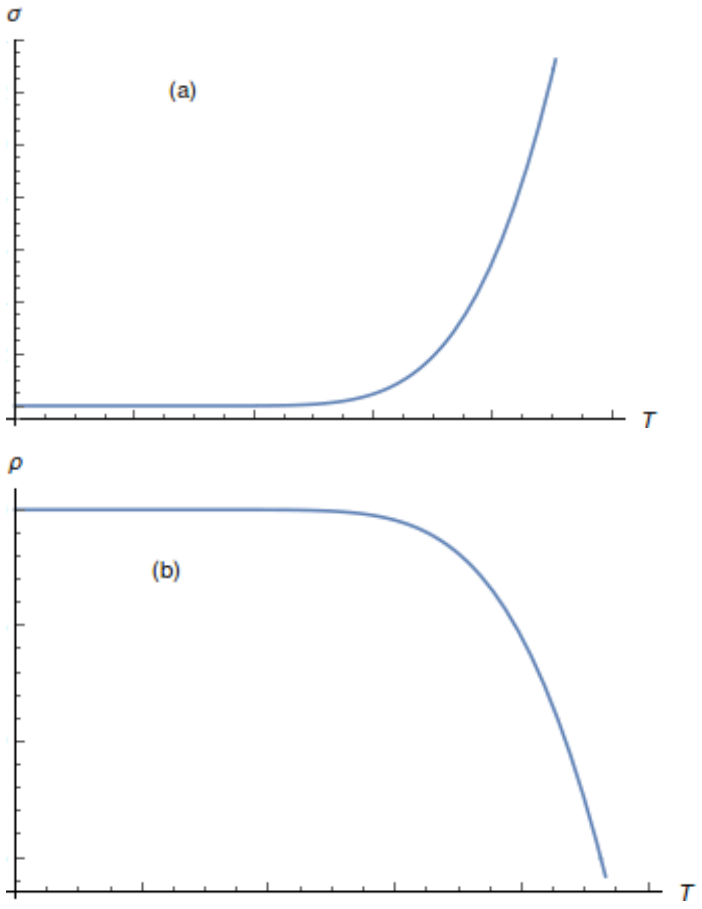

Figure 4.2: (a) Temperature dependence of the electrical conductivity based on Eq. 4.2. (b) Temperature dependence of the electrical resistivity based on Eq. 4.3. (arbitrary units).

4.1.2 Surface conductor (topological insulator)

In this case, the conductivity σ depends on the position $\vec{r}$. We will have a bulk conductivity σ_{bulk} when $\vec{r}$ is located in the bulk and a surface conductivity $\sigma_{surface}$

when $\vec{r}$ is at or near the surface. We assume that the bulk conductivity is activated,

$$\sigma_{bulk} = \sigma_0 \exp^{\frac{-E_g}{K_B T}}, \tag{4.5}$$

and the surface conductivity is

$$\sigma_{surface} = \sigma_s. \tag{4.6}$$

The total conductance of a sample is a combination between bulk and surface conductivity. The bulk conductivity depends on the temperature, while the surface conductivity does not. At low temperature, the bulk conductivity will be negligible compared to surface.

Then since $\rho(\vec{r}) = \frac{1}{\sigma(\vec{r})}$, we have

$$\rho_{bulk} = \frac{1}{\sigma_{bulk}} = \frac{\exp^{\frac{E_g}{K_B T}}}{\sigma_0}, \tag{4.7}$$

$$\rho_{surface} = \frac{1}{\sigma_{surface}} = \frac{1}{\sigma_s}. \tag{4.8}$$

Because the resistivity depends on the position, there is no simple proportionality relation between ρ and the total resistance R. R can only be found by measurement or by numerical method.

4.2 Numerical method

In order to find the relation between $\rho(x)$ and the total resistance R, we will review Maxwell's equations in Gaussian units (CGS).

Gauss's law for electric field:

$$\nabla \cdot \mathbf{E} = 4\pi\rho \tag{4.9}$$

Gauss's law for magnetic field:

$$\nabla \cdot \mathbf{B} = 0 \tag{4.10}$$

Maxwell-Faraday equation:

$$\nabla \times \mathbf{E} = -\frac{1}{c}\frac{\partial \mathbf{B}}{\partial t} \tag{4.11}$$

Ampère-Maxwell equation:

$$\nabla \times \mathbf{B} = \frac{4\pi}{c}J + \frac{1}{c}\frac{\partial \mathbf{E}}{\partial t}. \tag{4.12}$$

The electric field $\vec{E}(x)$ also can be written in terms of the electric potential V,

$$\vec{E}(x) = -\nabla V(x). \tag{4.13}$$

Ohm's law is given as

$$\vec{J}(x) = \sigma(x)\vec{E}(x), \tag{4.14}$$

when $\vec{J}$ is the current density.

From equations 4.13 and 4.14 we have:

$$\vec{J}(x) = -\sigma(x)\nabla V(x). \tag{4.15}$$

We also need the continuity equation which is given by,

$$\nabla \cdot \vec{J} = 0 \tag{4.16}$$

or

$$\vec{\nabla} \cdot (-\sigma(x)\nabla V(x)) = 0, \tag{4.17}$$

The system is subject to the following boundary conditions. First, we assume

that there is no current perpendicular to the boundaries, except where the current enters or leaves the sample. The voltage is fixed where the voltage leads are attached to the sample.

I used the relaxation method to solve for the voltage $V(x)$ using Eq. (4.17) and the boundary conditions described above. To implement this, I wrote equations for all parts of the system (corners, faces, edges, and the bulk) in discrete form. These equations are given in the Appendix. The relaxation method is an iterative method that is used to solve partial differential equations. It begins with a set of arbitrary voltages at each point in the sample, except at those points where the voltage is fixed (at the input and output leads). The voltage at every point is recalculated using the continuity equation Eq. (4.17). This process is repeated until the the system has relaxed (the voltage stops changing with each iteration).

I developed code using the Mathematica program. In my simulation, a thin $l_x = l_y = \frac{l_z}{10}$ sample was used, with input and output leads at the centres of the largest faces (the top and bottom). A grid size of 50$\times$ 50$\times$ 50 was used. Different initial voltage configurations were tested, including random, constant and smoothly increasing. The random and constant initial configurations resulted in very slow relaxation, so I used the smooth increase between the bottom face set at $V = 0$ and the top face set at $V = V_{\text{out}}$ for my initial voltage configuration.

After testing the program, I determined that 50,000 iterations were required for the system to relax. This took about 120 hours for each one, depending on the machine. Initial tests were run on the first year physics lab computers and on a machine owned by Dr. Plumer. The final results were collected on my own computer.

4.3 Resistance and resistivity of SmB_6: fits

4.3.1 Resistance and resistivity calculation using experimental data

4.3.1.1 Data 1

In experimental work [60], M. C. Hatnean et al. reported the resistivity of SmB_6 as a function of temperature. This is a little unusual, as normally the resistance and not resistivity measurements are reported. The resistivity must be inferred by by taking into account the sample geometry. They used large, high quality single crystals in their experiments, which were prepared by floating zone technique. They cut a bar-shaped sample from the SmB_6 crystal for their resistivity measurements. In this section, we examine whether the experimental data is better described by the non-topological insulator case or the topological insulator case.

We first consider case 1: non-topological insulator. In order to find the values of σ_a, σ_b, and E_g, we use their data and fit it to Eq. 4.4. The result of our fit are $\frac{\sigma_a}{C}$ = 0.0391 $\pm$0.0002 ohm $^{-1}$, $\frac{\sigma_b}{C}$ =4200 $\pm$900 ohm $^{-1}$, and E_g = 53.3$\pm$0.9 K (4.6 $\pm$0.4 meV). Because of the elongated shape of the sample we assume that $R = \rho\frac{L}{A}$, where L is the length, A is cross-sectional area of the sample, and $C = \frac{L}{A}$.

In second case, of topological insulator (ie, surface conductor), and due to the sample shape Fig 4.4, the surface and bulk resistance equations take a formula of two resistances as R_1 and R_2 connected in parallel,

$$R = \frac{R_1 \times R_2}{R_1 + R_2} \tag{4.18}$$

where R_1 is the surface resistance and R_2 is the bulk resistance.

The surface resistance is

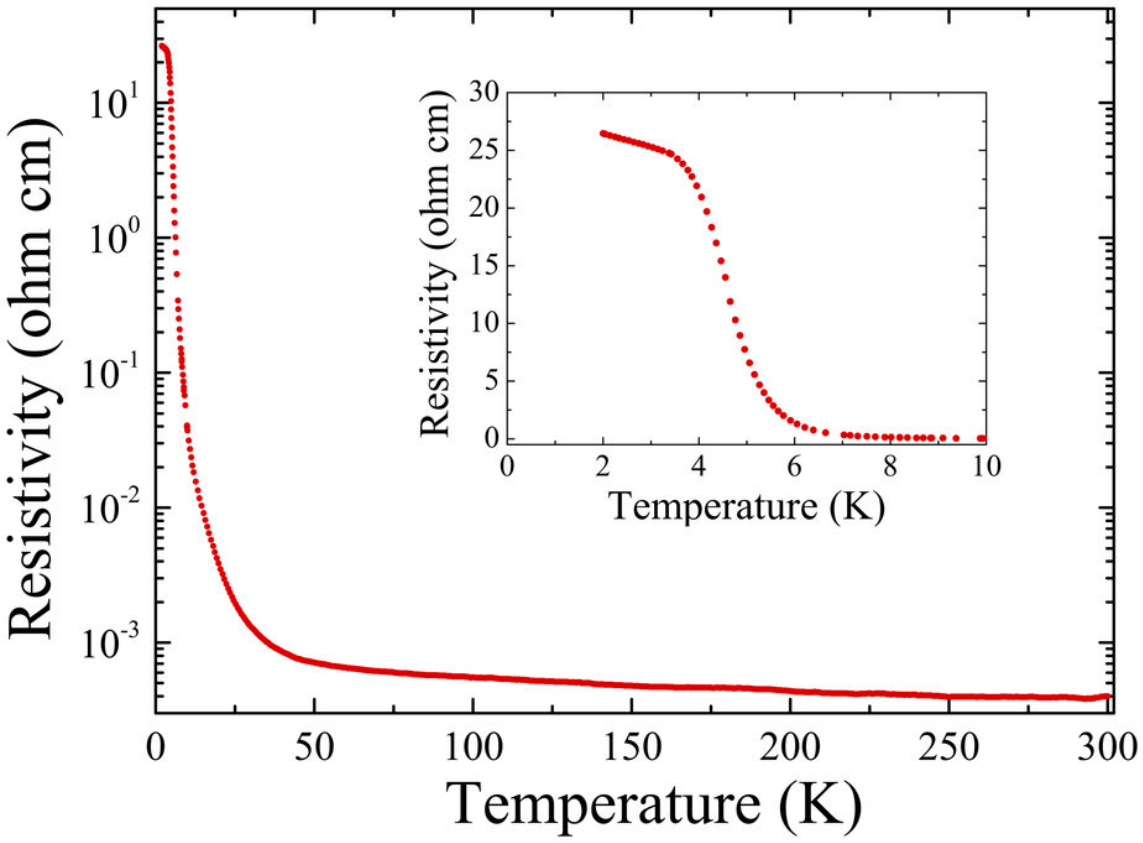

Figure 4.3: Experimental data shows the resistivity vs temperature (reproduced from Ref. [60]).

$$R_1 = \frac{L}{A_1}\rho_{surface} \tag{4.19}$$

and the bulk resistance is

$$R_2 = \frac{L}{A_2}\rho_{bulk}, \tag{4.20}$$

where L is the length of the sample, A_1 is the cross-sectional area of the surface, A_2 is the cross-sectional area of the bulk, and $A_2 \gg A_1$.

As before,

$$\rho_{surface} = \frac{1}{\sigma_s} \tag{4.21}$$

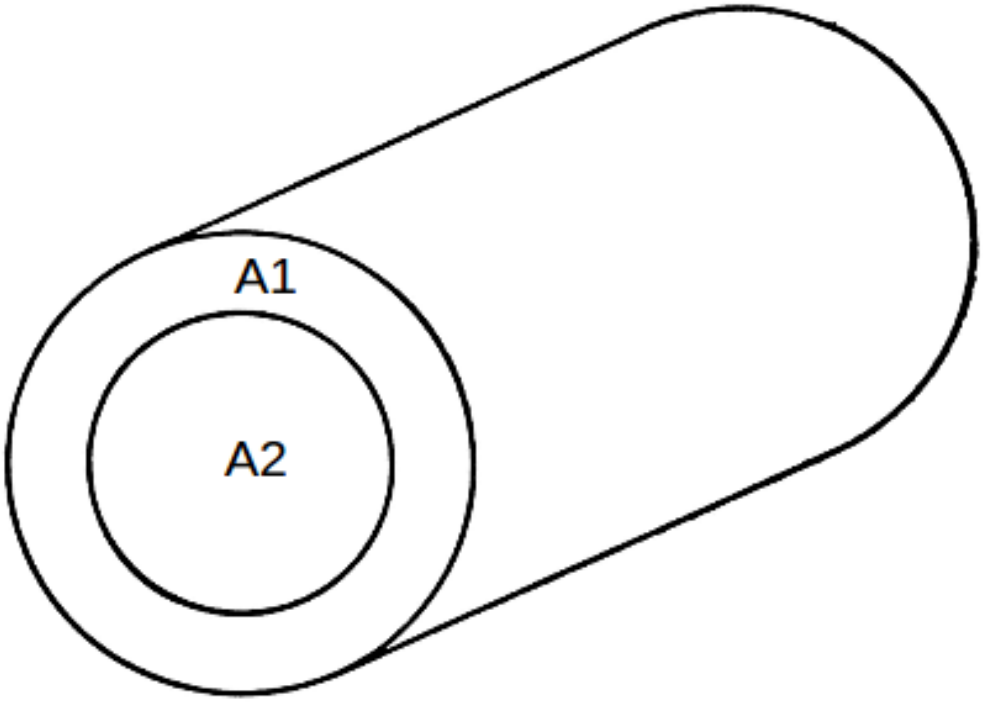

Figure 4.4: Schematic picture for the thin and elongated sample shape used. A_1 is the cross-sectional area of the surface, A_2 is the cross-sectional area of the bulk. In a real sample $A_1 \ll A_2$.

$$\rho_{bulk} = \frac{1}{\sigma_{bulk}} = \frac{\exp^{\frac{E_g}{T}}}{\sigma_0}. \tag{4.22}$$

Then the total resistance is

$$R = \frac{L\rho_{surface}\rho_{pulk}}{A_2\rho_{surface} + A_1\rho_{pulk}} \tag{4.23}$$

$$= \frac{1}{\frac{A_1\sigma_s}{L} + \frac{A_2\sigma_0 \exp^{\frac{-E_g}{T}}}{L}}. \tag{4.24}$$

We fit the experimental data to $R = \frac{1}{c_1 + c_2 \exp^{\frac{-E_g}{T}}}$ to get the unknown values which

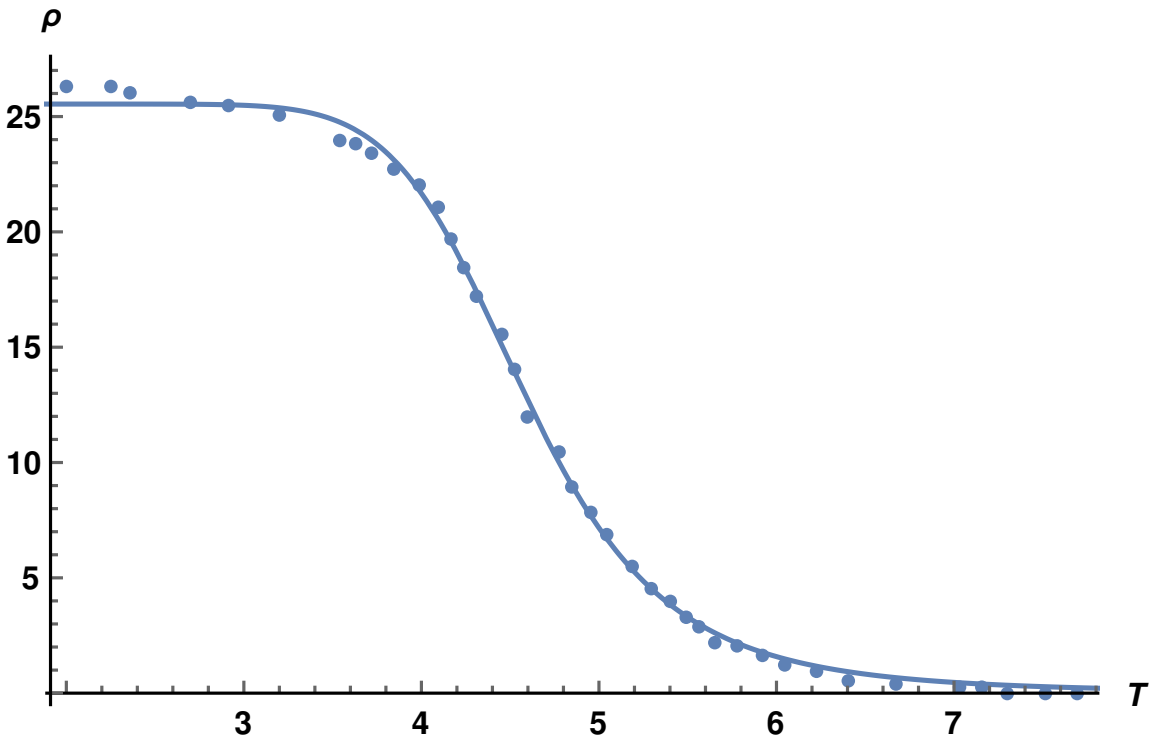

Figure 4.5: Resistivity vs temperature for a bar shaped sample of SmB_6. The dots are data points extracted from Ref. [60], and the solid line is the fit to Eq.4.4.

is exactly the same form as for the bulk conductivity case. As a result, we find that $\frac{A_1\sigma_s}{L} = c_1 = 0.0391 \pm 0.0002$ ohm $^{-1}$, $\frac{A_2\sigma_0}{L} = c_2 = 4200 \pm 900$ ohm $^{-1}$, and $E_g = 53.3$ ± 0.9 K (4.6 ± 0.4meV). Then by using these values in Eq. 4.24, we will have the same graph that is shown in Fig 4.5.

4.3.1.2 Data 2

Another experimental work [55], (described above) has studied the transport properties of SmB_6 with a specialized sample geometry to find the resistivity at low temperature. We study this data to see if it is described by the case of a non-topological insulator (bulk conductor).

To find the values of $\frac{\sigma_a}{C}$, $\frac{\sigma_b}{C}$, and E_g, we use their data and fit it to Eq. 4.4. The results of the fit are $\frac{\sigma_a}{C} = 0.262 \pm 0.003$ ohm $^{-1}$, $\frac{\sigma_b}{C} = 1200 \pm 400$ ohm $^{-1}$ and $E_g =$

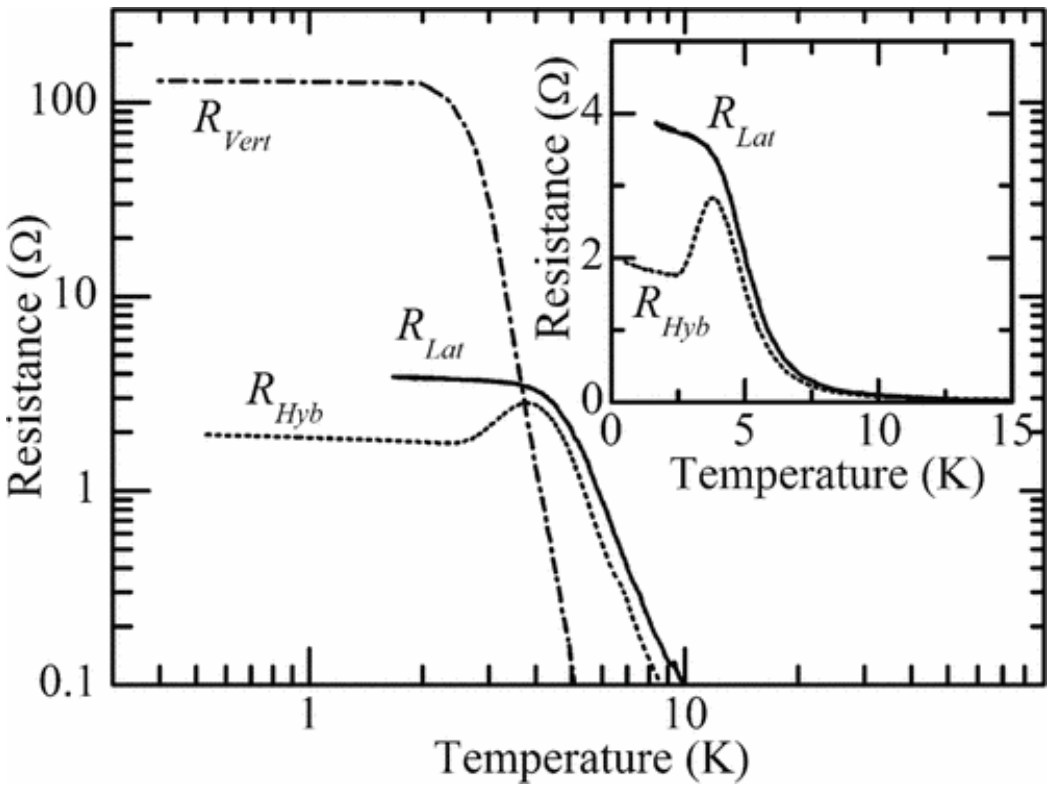

Figure 4.6: Experimental data shows the resistivity vs temperature for various configurations of voltage and current contacts. (Reproduced from Ref. [55] with permission).

43.03 ±1.82 K (3.71 ±0.16 meV). Figure 4.7 shows the resistance vs. temperature of data and fit, where we fit this data using the bulk conductor model (Eq. 4.4).

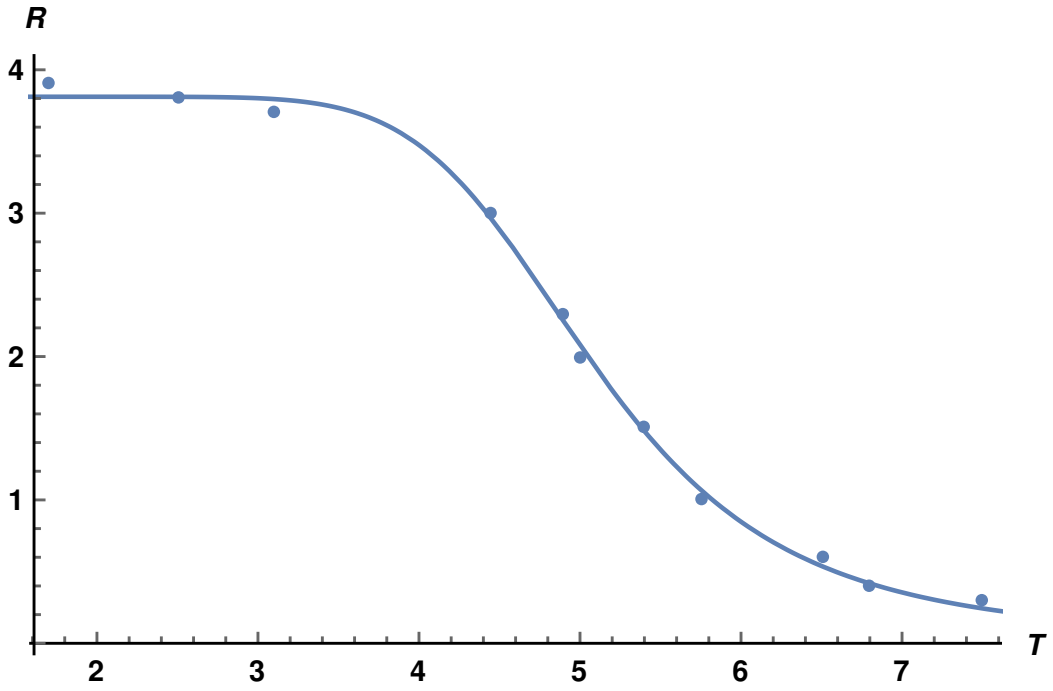

Figure 4.7: Resistance vs temperature. The dots are data points extracted from Ref. [55], and the solid line is the fit to Eq. 4.5 (case of non-topological insulator, bulk conductor).

4.3.2 Resistance and resistivity calculation for a surface conductor

We use a numerical relaxation method to calculate the resistance of a thin surface conducting sample with current and voltage leads at the same place (on the front and back faces of the sample). We set all the currents perpendicular to the boundary to be zero, except where the current comes in or out; the voltage is also fixed at these points. Also, the conductivity that we use is a function of the temperature and position. As discussed in Section 4.2, I solved Eq. 4.17 numerically, using the discrete equations given in the Appendix.

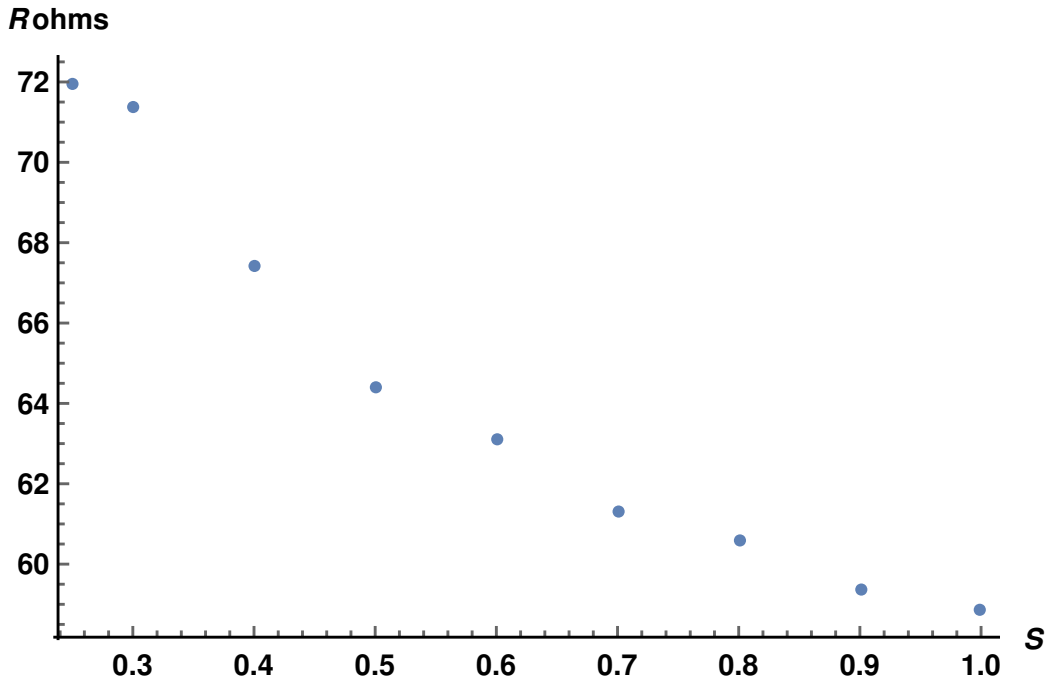

Figure 4.8: Resistance vs S in our calculation.

We introduce the parameter $S = \frac{\sigma_{bulk}}{\sigma_{surface}}$, the ratio of bulk conductivity, and surface conductivity and we performed our calculation using the specific of values of S (1, 0.9, 0.8, 0.7, 0.6, 0.5, 0.4, 0.3, 0.25).

The temperature is related to the value of S as

$$S = \frac{\sigma_{bulk}}{\sigma_{surface}} \tag{4.25}$$

$$= \frac{\sigma_0 exp^{\frac{-E_g}{K_B T}}}{\sigma_s}. \tag{4.26}$$

Then

$$T = \frac{E_g}{-\log(S) + \log(\frac{\sigma_0}{\sigma_s})}. \tag{4.27}$$

We cannot calculate the temperature T, because we do not know the value of $\frac{\sigma_0}{\sigma_s}$, but we can use Eq. (4.27) to illustrate the temperature dependence of R using an estimated value of $\frac{\sigma_0}{\sigma_s}$.

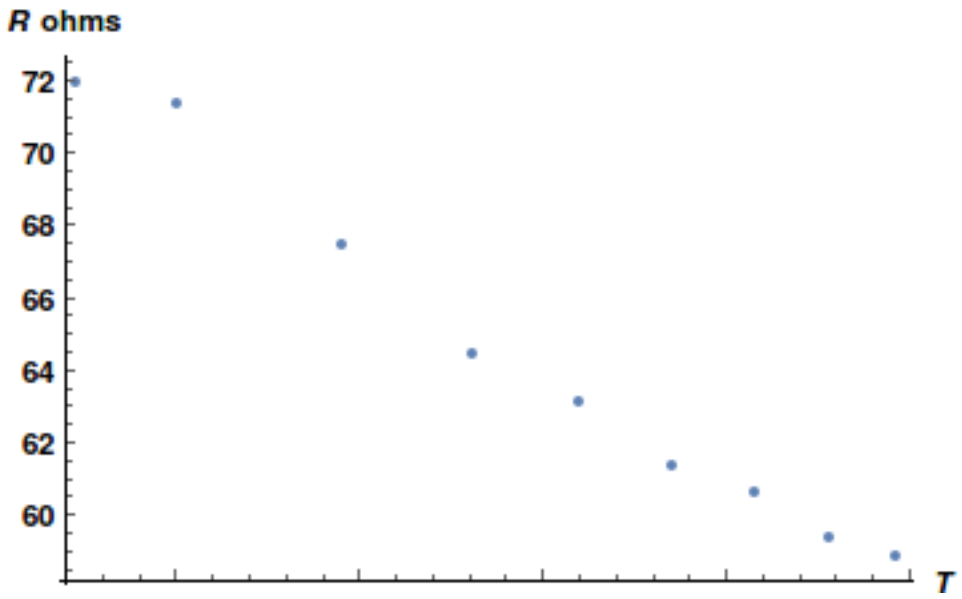

Figure 4.9: Resistance vs temperature in our fits, by using an estimated values of $\frac{\sigma_0}{\sigma_s}$.

This plot shows the correct qualitative dependence of the resistance R or temperature, as found in the measurements. (Fig 4.6, R_{lat} curve.)

S. Wolgast et al. [55], argued that SmB_6 becomes a surface conductor at low temperature based on their measurements behavior of different configurations as shown

in Fig 4.6. As we discussed before, R_{lat} configuration the current flow similar in both scenarios, which make it difficult to distinguish between surface dominated and bulk dominated conduction in this configuration alone. However, R_{vert} in a surface conductor is larger than it is in the bulk conductor. Also, R_{hyb} at high-temperature in both cases will be identical to R_{lat}, but at low-temperature, $R_{hyb} > R_{lat}$ in the surface dominated conduction, and it will still be identical to R_{lat} in bulk dominated conduction.

Both experiments [55, 60] conclude that SmB_6 is a surface conductor. We find that their data described by either bulk or surface conductance; however, we did not examine all the different voltage and current leads configurations. However, even if the conductance is on the surface, that does not mean that SmB_6 is a topological insulator, because there are other origins of surface conductivity, as we discuss in Chapters 5 and 6.

Chapter 5

Discussion

SmB_6 is a fully three-dimensional material with strong electron correlations. It's $4f$ electrons are hybridized with the $5d$ conduction band at around 50 K where SmB_6 goes through metal to insulator transition. Most importantly, at temperatures below 3 K the resistivity saturates and remains finite as T $\longrightarrow$ 0. This material has been investigated by a number of recent spectroscopy, quantum oscillation (Chapter 3), resistivity (Chapter 4) and measurements, as well as angle-resolved photoemission spectroscopy (ARPES) and scanning tunneling microscopy (STM) experiments.

5.1 Quantum oscillation of SmB_6

In Chapter 3 we examine the results of de Haas van Alphen measurements of the Fermi surface of SmB_6. We showed that even if there is a surface that is compatible with a 2D Fermi surface, the χ^2 values and the values of a and c in the 3D fits of some surfaces indicate the Fermi surfaces arise from 3D ellipsoidal shaped Fermi surface centered around the X-point of the Brillioun zone.

5.2 Resistivity of SmB_6

In the previous Chapter, we studied experimental measurements of the resistivity of SmB_6 [55,60]. The resistance as a function of temperature fits well to either the bulk conducting or surface conducting models. However, the studies of S. Wolgast et al, who measured the resistance for different voltage and current contact configurations, showed that SmB_6 becomes a surface conductor at low temperature based on their measurements using of different configurations of voltage and current contacts. Where R_{lat} is similar to R_{hyb} at high temperature, while at low temperature $R_{lat} > R_{hyb}$. Also, R_{vert} showed the largest curve at low temperature. Further modeling of the exact setups they used would be helpful to confirm this.

Polishing and etching the sample also affects the resistance [63]. Polishing and etching may damage the surface, producing cracks, which increases the surface conductivity. This has led to the proposal that surface conductivity could be due to "dangling p-bonds" will cause some change and decrease the resistivity.

5.3 Angle-resolved photoemission spectroscopy

5.3.1 Brief description of ARPES

Photoemission spectroscopy depends on the photoelectric effect, originally observed by Hertz (1887) and later explained by Einstein's photoelectric effect equation (1905). He recognized that when light with energy $h\nu$ (where h is Plank's constant and ν is the frequency of the light) shines on a sample with work function ϕ, an electron can absorb a photon and get away of the material with a maximum energy (kinetic energy) $E_{kin} = h\nu - \phi$. Thus photo-electron spectroscopy can measure the energy of an electron inside a solid. In addition, the momentum of the electrons can also

be obtained where $p = \sqrt{2mE_{kin}}$, and different momentum electrons will escape at different angles from the surface of a material [64].

Angle-resolved photoemission spectroscopy (ARPES) can examine the electronic structure of the surface state and the low energy excitations of solids. Although, the spin-resolved ARPES can investigate the spin structure of the surface state, these spin structure still has some argument because of the limited energy resolution of ARPES comparative to the small Kondo gap of SmB_6. The results of spin-polarized ARPES studies are still controversial due to a highly challenging measurement that comes from the narrowness of the bulk insulating gap. For more details and description of ARPES see Ref. [67].

5.3.2 ARPES studies on SmB_6

Recently, there are many ARPES studies on SmB_6. One of them is Neupane et al. [34] who find the surface electronic structure of topological Kondo SmB_6. Other important results were provided by N. Xu et al. [10], and J. Jiang et al. [9] at the same time, whose their experimental results established that SmB_6 is the first realization of a three-dimensional topological Kondo insulator.

On the other hand, Z. H. Zhu et al. [68] combined the ARPES with density functional theory calculations. They concluded that the surface state of SmB_6 has a metallic property because of polarity. In other words, they suggested that a conducting surface state of SmB_6 originates from boron bonds located in the (001) crystal surface, which is a non-topological polar surface.

5.4 Scanning Tunneling Microscopy

Scanning tunneling microscopy (STM) is another useful surface states probe; it is a tool that obtains the atoms images on the surfaces of materials. The STM was developed in 1982 by Gerd Binnig and Heinrich Rohrer and they won Nobel Prize (1986) in physics. STM data use the color scale to provide spatial information about variations in electron tunneling current values on very small length scale. STM detects the irregularities produced by the electrons surrounding the atoms on the surface by the probe and the resistance is mapped by a computer into an image. See reference [65] for a more detailed description of STM.

5.4.1 STM studies of the surface state of SmB_6

STM has played an important role in discovering the new physics in both topological insulators and Kondo lattices. It is thus an ideal probe for showing the electronic structure evolution of SmB_6 and the existence of a topological surface state.

As recently as 2013, Yee et al. [50], confirmed that SmB_6 is a Kondo insulator, where they inserted the cleaved surface of SmB_6 sample into scanning tunneling microscopy. They also observed that at lowest temperatures the remaining spectral weight crossing the hybridization gap, which make them think that may consistent with a topological surface state.

Similar to Yee et al., Ruan et al. [66] found the temperature dependence of the surface space spectra in which the hybridization gap opens at temperatures above 60 K and the emergence of a collective in-gap resonance at $T < 40$ K. Although the low-temperature behavior may come from a topological surface state, STM has not provided enough evidence to show that SmB_6 is a topological Kondo insulator [30].

Very recently, some experiments injected spin-polarized tunneling electrons into a

topological insulator sample to study the spin of topological insulators, and to examine the energy dependence of the effective spin polarization at the topological surface. As a result, they verified a large spin polarization for topological insulator materials.

In this Chapter, we summarized the main experiments that examined SmB_6. Some of their results provide direct evidence of SmB_6 metallic surface states at the low temperature. This metallic surface states does not necessarily indicate that SmB_6 is a topological insulator. The presence of boron dangling bonds on a polar surface could also lead to a metallic surface in SmB_6.

Chapter 6

Conclusions

The overall objective of this work was to examine whether there is enough experimental evidence to conclude that SmB_6 is a topological insulator or not. We discussed the topological insulator phenomenon and the properties of samarium hexaboride (SmB_6), and we find that this aspect contains many physics problems.

Our fits of de Haas-van Alphen measurements shows the possibility of having either a 3D ellipsoidal shape or a 2D Fermi surface. Therefore, dHvA cannot tell if SmB_6 has surface or bulk conductance. Also, the resistance calculations show that the resistance function fits well to both the bulk conducting and surface conducting models. However, using different configurations of voltage and current contacts demonstrates that the conductivity is most likely on the surface. In another word, we think it is most likely that SmB_6 has a metallic surface state.

The existence of a metallic surface state in SmB_6 could be due to the topological surface properties. However, there is not enough evidence to say that SmB_6 is indeed a topological insulator, since even if the conductivity comes from the surface, it does not mean that SmB_6 is a topological insulator. This conductivity could be because of the general property of hexaborides (boron dangling bonds) on a polar surface, or because

of any other reason. The experiments that can tell if the SmB_6 has a topological insulator properties are those which measure the spin surface and spin polarization, spin polarized conductance spectroscopy or study the experiments that can detect dangling bonds. A definite answer will come when we have enough experiments that study the surface state properties.

Bibliography

[1] B. Andrei Bernevig, *Topological Insulators and Topological Superconductors* (Princeton, New Jersey, 1978).

[2] Richard E. Prange and Steven M. Girvin, *The Quantum Hall Effect* (Springer-Verlag, New York, 1990).

[3] X. L. Qi and S. C. Zhang, "The quantum spin Hall effect and topological insulators," Physics Today **63**, 3-38 (2010).

[4] Yoichi Ando, "Topological Insulator Materials," J. Phys. Soc. Jpn. **82**, 102001 (2013).

[5] Barry R. Holstein, "The adiabatic theorem and Berry's phase," Am. J. Phys. **57**, 12 (1988).

[6] X. L. Qi, and S. C. Zhang, "Topological insulators and superconductors," Rev. Mod. Phys. **83**, 1057-1110 (2011).

[7] C. L. Kane, and E. J. Mele, "Z_2 Topological Order and the Quantum Spin Hall Effect," Phys. Rev. Lett. **95**, 146802 (2005).

[8] X. L. Qi, T. L. Hughes, and S. C. Zhang, "Topological field theory of time-reversal invariant insulators," Phys. Rev. B **78**, 195424 (2008).

[9] H. Jiang, S. Cheng, Q. f. Sun, and X. C. Xie, "Topological Insulator: A New Quantized Spin Hall Resistance Robust to Dephasing," Phys. Rev. Lett. **103**, 036803 (2009).

[10] S. Y. Xu, *Discoveries of New Topological States of Matter Beyond Topological Insulators* (Ph. D. Thesis), University of Princeton (2015).

[11] L. Fu, C. L. Kane, and E. J. Mele, "Topological Insulators in Three Dimensions," Phys. Rev. Lett. **98**, 106803 (2007).

[12] S. H. Chen, B. K. Nikoli, and C. R. Chang, "Inverse quantum spin Hall effect generated by spin pumping from precessing magnetization into a graphene-based two-dimensional topological insulator," Phys. Rev. B **81**, 035428 (2010).

[13] J. E. Moore, "The birth of topological insulators," Nature **464**, 194 (2010).

[14] R. Roy, "Topological phases and the quantum spin Hall effect in three dimensions," Phys. Rev. B **79**, 195322 (2009).

[15] H. Zhang, C. X. Liu, X. L. Qi, X. Dai, Z. Fang, and S. C. Zhang, "Topological insulators in Bi_2Se_3, Bi_2Te_3 and Sb_2Te_3 with a single Dirac cone on the surface," Nature Physics **5** (2009).

[16] D. Hsieh, Y. Xia, D. Qian, L. Wray, J. H. Dil, F. Meier, J. Osterwalder, L. Patthey, J. G. Checkelsky, N. P. Ong, A. V. Fedorov, H. Lin, A. Bansil, D. Grauer, Y. S. Hor, R. J. Cava, and M. Z. Hasan, "A tunable topological insulator in the spin helical Dirac transport regime," Nature **460**, 1101-1105 (2009).

[17] M. Koenig, S. Wiedmann, C. Bruene, A. Roth, H. Buhmann, L. W. Molenkamp, X. L. Qi, and S. C. Zhang, "Quantum spin hall insulator state in HgTe quantum wells," Science **318** (2007).

[18] D. Hsieh, D. Qian, L. Wray, Y. Xia, Y. S. Hor, R. J. Cava, and M. Z. Hasan, "A topological Dirac insulator in a quantum spin Hall phase," Nature **452**, 970 (2008).

[19] J. C. Y. Teo, L. Fu, and C. L. Kane, "Surface states and topological invariants in three-dimensional topological insulators: Application to $Bi_{1-x}Sb_x$," Phys. Rev. B **78**, 045426 (2008).

[20] M. Z. Hasan, S. Y. Xu, and M. Neupane, "Topological Insulators, Topological Crystalline Insulators, and Topological Kondo Insulators," arXiv:1406.1040 (2015).

[21] M. Dzero, J. Xia, V. Galitski, and P. Coleman, "Topological Kondo Insulators," arXiv:1506.05635 (2015).

[22] B. A. Bernevig and S. C. Zhang, "Quantum Spin Hall Effect," Phys. Rev. Lett. **96**, 106802 (2006).

[23] B. A. Bernevig, T. L. Hughes, and S. C. Zhang, "Quantum Spin Hall Effect and Topological Phase Transition in HgTe Quantum Wells," Science **314** (2006).

[24] C. L. Kane and E. J. Mele, "Z_2 Topological Order and the Quantum Spin Hall Effect," Phys. Rev. Lett. **95**, 146802 (2005).

[25] A. Roth, C. Bruene, H. Buhmann, L. W. Molenkamp, J. Maciejko, X. L Qi, and S. C. Zhang, "Nonlocal Transport in the Quantum Spin Hall State," Science, **325** (2009).

[26] L. Fu and C. L. Kane, "Topological insulators with inversion symmetry," Phys. Rev. B **76**, 045302 (2007).

[27] J. E. Moore and L. Balents, "Topological invariants of time-reversal-invariant band structures," Phys. Rev. B **75**, 121306 (2007).

[28] D. Hsieh, D. Qian, L. Wray, Y. Xia, Y. S. Hor, R. J. Cava, and M. Z. Hasan, "A topological Dirac insulator in a quantum spin Hall phase," Nature **452** (2008).

[29] V. Alexandrov, M. Dzero, and P. Coleman, "Cubic Topological Kondo Insulators," Phys. Rev. Lett. **111**, 226403 (2013).

[30] M. Dzero, K. Sun, V. Galitski, and P. Coleman, "Topological Kondo Insulators," Phys. Rev. Lett. **104**, 106408 (2010).

[31] N. Xu, X. Shi, P. K. Biswas, C. E. Matt, R. S. Dhaka, Y. Huang, N. C. Plumb, M. Radovic, J. H. Dil, E. Pomjakushina, K. Conder, A. Amato, Z. Salman, D. McK. Paul, J. Mesot, H. Ding, and M. Shi., "Surface and bulk electronic structure of the strongly correlated system SmB_6 and implications for a topological Kondo insulator," Phys. Rev. B **88**, 121102(R), (2013).

[32] Tetsuya Takimoto, "SmB_6: A Promising Candidate for a Topological Insulator," J. Phys. Soc. Jpn. **80**, 123710 (2011).

[33] R. Yu, H. Weng, X. Hu, Z. Fang, and X. Dai., "Model Hamiltonian for topological Kondo insulator SmB_6," New J. Phys. **17**, 023012 (2015).

[34] M. Neupane, N. Alidoust, S-Y. Xu, T. Kondo, Y. Ishida, D. J. Kim, Chang Liu, I. Belopolski, Y. J. Jo, T-R. Chang, H-T. Jeng, T. Durakiewicz, L. Balicas, H. Lin, A. Bansil, S. Shin, Z. Fisk, and M. Z. Hasan. "Surface electronic structure of the topological Kondo-insulator candidate correlated electron system SmB_6," Nature Commun. **4**, 2991 (2013).

[35] V. Antonov, B. Harmon, and A. Yaresko, *Electronic Structure and Magneto-Optical Properties of Solids* (Kluwer Academic Publishers. Dordrecht, 2004).

[36] V. N. Antonov and B. N. Harmon, "Electronic structure of mixed-valence semiconductors in the LSDA+U approximation. II. SmB_6 and YbB_{12}," Phys. Rev. B **66**, 165209 (2002).

[37] A. Yanase and H. Harima, "Band Calculations on YbB_6, SmB_6 and CeNiSn," Prog. Theor. Phys. **108**, 19-25 (1992).

[38] C. J. Kang, J. Kim, K. Kim, J.-S. Kang, J. D. Denlinger, and B. I. Min., "Band Symmetries of Mixed-Valence Topological Insulator: SmB_6," J. Phys. Soc. Jpn. **84**, 024722 (2015).

[39] M. Tinkham, *Group Theory And Quantum Mechanics* (New York, 1964).

[40] J. Iaconis and L. Balents, "Many-body effects in topological Kondo insulators," Phys. Rev. B **91**, 245127 (2015).

[41] V. Alexandrov, P. Coleman, and O. Erten, "Kondo Breakdown in Topological Kondo Insulators," Phys. Rev. Lett. **114**, 177202 (2015).

[42] F. Lu, J. Zhao, H. Weng, Z. Fang, and X. Dai, "Correlated Topological Insulators with Mixed Valence," Phys. Rev. Lett. **110**, 096401 (2013).

[43] A. Menth, E. Buehler, and T. Geballe, "Magnetic and Semiconducting Properties of SmB_6," Phys. Rev. Lett. **22** (1969).

[44] B. S. Tan, Y. T. Hsu, B. Zeng, M. C. Hatnean, N. Harrison, Z. Zhu, M. Hartstein, M. Kiourlappou, A. Srivastava, M. D. Johannes, T. P. Murphy, J. H. Park, L. Balicas, G. G. Lonzarich, G. Balakrishnan, and S. E. Sebastian, "Heavy

fermions. Unconventional Fermi surface in an insulating state," Science **349**, 287 (2015).

[45] G. Li, Z.Xiang, F.Yu, T. Asaba, B. Lawson, P. Cai, C. Tinsman, A. Berkley, S. Wolgast, Y. Eo, D. Kim, C. Kurdak, J. W. Allen, K. Sun, X. Chen, Y. Y. Wang, Z. Fisk, and L. Li, "Two-dimensional Fermi surfaces in Kondo insulator SmB_6," Science **346**, 1208-12(2014).

[46] D. Shoenberg, "Evidence from the de Haas-van Alphen effect," Phys. Kondens. Materie **9**, 1-14 (1969).

[47] Z. Yue, X. Wang, D. Wang, J. Wang, D. Culcer, and S. Dou, "Crossover of magnetoresistance from fourfold to twofold symmetry in SmB_6 single crystal, a topological Kondo insulator," J. Phys. Soc. Jpn. **84**, 044717 (2015).

[48] A. J. Schofield, " Non-Fermi liquids," Contemp. Phys. **40**, 95–115 (1999).

[49] S. Behler and K.Winzer, "De Haas-van Alphen effect in rare-earth hexaborides (RE=Pr, Nd, Gd)," Z. Phys. B-Condens. Matter **82**, 355–361 (1991).

[50] M. M. Yee, Y. He, A. Soumyanarayanan, D. J. Kim, Z. Fisk, and J. E. Hoffman, "Imaging the Kondo Insulating Gap on SmB_6," arXiv:1308.1085 (2013).

[51] A. McCollam, J. S. Xiab, J. Flouquet, D. Aoki, and S. R. Julian, "De Haas van Alphen effect in heavy fermion compounds-effective mass and non-Fermi-liquid behaviour," Physica B **403**, 717–720 (2008).

[52] U. Mizutani, *Introduction to the Electron Theory of Metals* (Cambridge University Press, United Kingdom, 2001).

[53] S. Curnoe and K. A. Kikoin, " 4 Electron self-trapping in intermediate-valent SmB_6," Phys. Rev. B **61**, 15714-15725 (2000).

[54] D. J. Kim, J. Xia, and Z. Fisk, "Topological surface state in the Kondo insulator samarium hexaboride," Nature Materials **13**, 466–470 (2014).

[55] S. Wolgast, C. Kurdak, K. Sun, J. W. Allen, D-J. Kim, and Z. Fisk., "Low-temperature surface conduction in the Kondo insulator SmB_6," Phys. Rev. B **88**, 180405(R) (2013).

[56] D. J. Kim, S. Thomas, T. Grant, J. Botimer, Z. Fisk, and J. Xia, "Surface Hall Effect and Nonlocal Transport in SmB_6: Evidence for Surface Conduction" . Scientific Reports **3**, 3150 (2013).

[57] S. Thomas, D. J. Kim, S. B. Chung, T. Grant, Z. Fisk, and J. Xia, "Weak Antilocalization and Linear Magnetoresistance in the Surface State of SmB_6," ArXiv1307.4133 (2003).

[58] Y. Luo, H. Chen, J. Dai, Z. Xu, and J. D. Thompson, "Heavy surface state in a possible topological Kondo insulator: Magnetothermoelectric transport on the (011) plane of $SmB6_6$," Phys. Rev. B **91**, 075130 (2015).

[59] F. Chen, C. Shang, Z. Jin, D. Zhao, Y. P. Wu, Z. J. Xiang, Z. C. Xia, A. F. Wang, X. G. Luo, T. Wu, and X. H. Chen, "Magnetoresistance evidence of a surface state and a field-dependent insulating state in the Kondo insulator $SmB6_6$," Phys. Rev. B **91**, 205133 (2015).

[60] M. C. Hatnean, M. R. Lees, D. M. K. Paul, and G. Balakrishnan, "Large, high quality single-crystals of the new Topological Kondo Insulator, $SmB6_6$", Scientific Reports **3**, 3071 (2013).

[61] N. Wakeham, J. Wena, Y. Q. Wanga, Z. Fiskc, F. Ronninga, and J. D. Thompson, "The effect of magnetic and non-magnetic ion damage on the surface state in SmB_6," J. Magn. Magn. Mater. **400**, 62–65 (2016).

[62] W. A. Phelan, S. M. Koohpayeh, P. Cottingham, J. W. Freeland, J. C. Leiner, C. L. Broholm, and T. M. McQueen, "Correlation between bulk thermodynamic measurements and the low temperature resistance plateau in SmB_6," Phys. Rev. X **4**, 031012 (2014).

[63] S. Gabani, G. Pristas, I. Takacova, N. Sluchanko, K. Siemensmeyer, N. Shitsevalova, V. Filipov, and K. Flachbart., "Surface and bulk components of electrical conductivity in (presumably special topological) Kondo insulator SmB_6 at lowest temperatures," Solid State Sci. **47,** 17-20 (2015).

[64] A. Damascelli, Z. Hussain, and Z. X. Shen, "Angle-resolved photoemission studies of the cuprate superconductors," Rev. Mod. Phys. **75** (2003).

[65] G. Binning, H. Rohrer, C. Gerber, and E. Weibel, "Surface Studies by Scanning Tunneling Microscopy," Phys. Rev. Lett. **49**, 57 (1982).

[66] W. Ruan, C. Ye, M. Guo, F. Chen, X. Chen, G. M. Zhang, and Y. Wang, "Emergence of a coherent in-gap state in the SmB_6 Kondo insulator revealed by scanning tunneling spectroscopy," Phys. Rev. Lett. **112**, 136401 (2014).

[67] W. Zhang, *Photoemission Spectroscopy on High Temperature Superconductors* (Springer-Verlag Berlin Heidelberg, 2013).

[68] Z. H. Zhu, A. Nicolaou, G. Levy, N. P. Butch, P. Syers, X. F. Wang, J. Paglione, G. A. Sawatzky, I. S. Elfimov, and A. Damascelli, "Polarity-Driven Surface Metallicity in SmB_6," Phys. Rev. Lett. **111**, 216402 (2013).

Appendix A

Numerical method

In chapter 4, I discussed the relaxation method that I work with, and which is subject to some boundary conditions. To solve the voltage $V(x)$, I wrote equations for all the system (corners, faces, edges, and the bulk) in discrete form using equations from 4.9 to 4.17 in Chapter 4.

I used n_x, n_y, n_z as a points on the grid, where $n_x = n_y = n_z = 50$. Also, I set the size of the sample as $l_x = l_y = 10$, and $l_z = 1$. Then, $dl_x = \frac{l_x}{n_x}$, $dl_y = \frac{l_y}{n_y}$, and $dl_z = \frac{l_z}{n_z}$.

A.1 corners:

$$V[1,1,1] = \frac{dl_x^2 {dl_y}^2 {dl_z}^2}{{dl_x}^2{dl_y}^2 + {dl_x}^2{dl_z}^2 + {dl_z}^2{dl_y}^2}\left(\frac{V[2,1,1]}{{dl_x}^2} + \frac{V[1,2,1]}{{dl_y}^2} + \frac{V[1,1,2]}{{dl_z}^2}\right) \quad \text{(A.1)}$$

$$V[n_x,1,1] = \frac{dl_x^2 {dl_y}^2 {dl_z}^2}{{dl_x}^2{dl_y}^2 + {dl_x}^2{dl_z}^2 + {dl_z}^2{dl_y}^2}\left(\frac{V[n_x-1,1,1]}{dl_x^2} + \frac{V[n_x,2,1]}{{dl_y}^2} + \frac{V[n_x,1,2]}{{dl_z}^2}\right) \quad \text{(A.2)}$$

$$V[1,n_y,1] = \frac{dl_x^2 {dl_y}^2 {dl_z}^2}{{dl_x}^2{dl_y}^2 + {dl_x}^2{dl_z}^2 + {dl_z}^2{dl_y}^2}\left(\frac{V[2,n_y,1]}{dl_x^2} + \frac{V[1,n_y-1,1]}{{dl_y}^2} + \frac{V[1,n_y,2]}{{dl_z}^2}\right) \quad \text{(A.3)}$$

$$V[1,1,n_z] = \frac{dl_x^2 {dl_y}^2 {dl_z}^2}{{dl_x}^2{dl_y}^2 + {dl_x}^2{dl_z}^2 + {dl_z}^2{dl_y}^2}\left(\frac{V[2,1,n_z]}{dl_x^2} + \frac{V[1,2,n_z]}{{dl_y}^2} + \frac{V[1,1,n_z-1]}{{dl_z}^2}\right) \tag{A.4}$$

$$\begin{aligned} V[n_x,n_y,1] = \frac{dl_x^2 {dl_y}^2 {dl_z}^2}{{dl_x}^2{dl_y}^2 + dlx^2{dl_z}^2 + {dl_z}^2{dl_y}^2}\Bigg(&\frac{V[n_x-1,n_y,1]}{dl_x^2} \\ &+ \frac{V[n_x,n_y-1,1]}{{dl_y}^2} + \frac{V[n_x,n_y,2]}{{dl_z}^2}\Bigg) \end{aligned} \tag{A.5}$$

$$\begin{aligned} V[n_x,1,n_z] = \frac{dl_x^2 {dl_y}^2 {dl_z}^2}{{dl_x}^2{dl_y}^2 + {dl_x}^2{dl_z}^2 + {dl_z}^2{dl_y}^2}\Bigg(&\frac{V[n_x-1,1,n_z]}{dl_x^2} \\ &+ \frac{V[n_x,2,n_z]}{{dl_y}^2} + \frac{V[n_x,1,n_z-1]}{{dl_z}^2}\Bigg) \end{aligned} \tag{A.6}$$

$$\begin{aligned} V[1,n_y,n_z] = \frac{dl_x^2 {dl_y}^2 {dl_z}^2}{{dl_x}^2{dl_y}^2 + {dl_x}^2{dl_z}^2 + {dl_z}^2{dl_y}^2}\Bigg(&\frac{V[2,n_y,n_z]}{dl_x^2} \\ &+ \frac{V[1,n_y-1,n_z]}{{dl_y}^2} + \frac{V[1,n_y,n_z-1]}{{dl_z}^2}\Bigg) \end{aligned} \tag{A.7}$$

$$\begin{aligned} V[n_x,n_y,n_z] = \frac{dl_x^2 {dl_y}^2 {dl_z}^2}{{dl_x}^2{dl_y}^2 + {dl_x}^2{dl_z}^2 + {dl_z}^2{dl_y}^2}\Bigg(&\frac{V[n_x-1,n_y,n_z]}{dl_x^2} \\ &+ \frac{V[n_x,n_y-1,n_z]}{{dl_y}^2} + \frac{V[n_x,n_y,n_z-1]}{{dl_z}^2}\Bigg) \end{aligned} \tag{A.8}$$

A.2 Edges:

$$\begin{aligned} &V[i,1,1] \\ &\quad = \frac{dl_x^2 {dl_y}^2 {dl_z}^2}{{dl_x}^2{dl_y}^2 + {dl_x}^2{dl_z}^2 + 2{dl_z}^2{dl_y}^2}\Bigg(\frac{V[i+1,1,1] + V[i-1,1,1]}{dl_x^2} \\ &\qquad\qquad + \frac{V[i,2,1]]}{{dl_y}^2} + \frac{V[i,1,2]]}{{dl_z}^2}\Bigg) \end{aligned} \tag{A.9}$$

$$V[i, n_y, 1] = \frac{dl_x^2 {dl_y}^2 {dl_z}^2}{{dl_x}^2 {dl_y}^2 + {dl_x}^2 {dl_z}^2 + 2{dl_z}^2 {dl_y}^2} \left(\frac{V[i+1, n_y, 1] + V[i-1, n_y, 1]}{dl_x^2} + \frac{V[i, n_y - 1, 1]]}{{dl_y}^2} + \frac{V[i, n_y, 2]]}{{dl_z}^2} \right) \tag{A.10}$$

$$V[i, 1, n_z] = \frac{dl_x^2 {dl_y}^2 {dl_z}^2}{{dl_x}^2 {dl_y}^2 + {dl_x}^2 {dl_z}^2 + 2{dl_z}^2 {dl_y}^2} \left(\frac{V[i+1, 1, n_z] + V[i-1, 1, n_z]}{dl_x^2} + \frac{V[i, 2, n_z]]}{{dl_y}^2} + \frac{V[i, 1, n_z - 1]]}{{dl_z}^2} \right) \tag{A.11}$$

$$V[i, n_y, n_z] = \frac{dl_x^2 {dl_y}^2 {dl_z}^2}{{dl_x}^2 {dl_y}^2 + {dl_x}^2 {dl_z}^2 + 2{dl_z}^2 {dl_y}^2} \left(\frac{V[i+1, n_y, n_z] + V[i-1, n_y, n_z]}{dl_x^2} + \frac{V[i, n_y - 1, n_z]]}{{dl_y}^2} + \frac{V[i, n_y, n_z - 1]]}{{dl_z}^2} \right) \tag{A.12}$$

$$V[1, i, 1] = \frac{dl_x^2 {dl_y}^2 {dl_z}^2}{{dl_x}^2 {dl_y}^2 + 2{dl_x}^2 {dl_z}^2 + {dl_z}^2 {dl_y}^2} \left(\frac{V[2, i, 1]}{dl_x^2} + \frac{V[1, i+1, 1] + V[1, i-1, 1]]}{{dl_y}^2} + \frac{V[1, i, 2]]}{{dl_z}^2} \right) \tag{A.13}$$

$$V[1, i, n_z] = \frac{dl_x^2 {dl_y}^2 {dl_z}^2}{{dl_x}^2 {dl_y}^2 + 2{dl_x}^2 {dl_z}^2 + {dl_z}^2 {dl_y}^2} \left(\frac{V[2, i, n_z]}{dl_x^2} + \frac{V[1, i+1, n_z] + V[1, i-1, n_z]]}{{dl_y}^2} + \frac{V[1, i, n_z - 1]]}{{dl_z}^2} \right) \tag{A.14}$$

$$V[n_x, i, 1] = \frac{dl_x^2 {dl_y}^2 {dl_z}^2}{{dl_x}^2 {dl_y}^2 + 2{dl_x}^2 {dl_z}^2 + {dl_z}^2 {dl_y}^2} \left(\frac{V[n_x - 1, i, 1]}{dl_x^2} + \frac{V[n_x, i+1, 1] + V[n_x, i-1, 1]}{{dl_y}^2} + \frac{V[n_x, i, 2]]}{{dl_z}^2} \right) \tag{A.15}$$

$$V[n_x, i, n_z] = \frac{dl_x^2 {dl_y}^2 {dl_z}^2}{{dl_x}^2 {dl_y}^2 + 2{dl_x}^2 {dl_z}^2 + {dl_z}^2 {dl_y}^2} \left(\frac{V[n_x - 1, i, n_z]}{dl_x^2} + \frac{V[n_x, i+1, n_z] + V[n_x, i-1, n_z]}{{dl_y}^2} + \frac{V[n_x, i, n_z - 1]]}{{dl_z}^2} \right) \tag{A.16}$$

$$V[1,1,i] = \frac{dl_x^2 {dl_y}^2 {dl_z}^2}{2{dl_x}^2 dly^2 + {dl_x}^2 dlz^2 + {dl_z}^2 {dl_y}^2} \left(\frac{V[2,1,i]}{dl_x^2} + \frac{V[1,1,i]}{{dl_y}^2} + \frac{V[1,1,i+1] + V[1,1,i-1]]}{{dl_z}^2} \right) \tag{A.17}$$

$$V[1,n_y,i] = \frac{dl_x^2 {dl_y}^2 {dl_z}^2}{2{dl_x}^2 {dl_y}^2 + {dl_x}^2 {dl_z}^2 + {dl_z}^2 {dl_y}^2} \left(\frac{V[2,n_y,i]}{dl_x^2} + \frac{V[1,n_y-1,i]}{{dl_y}^2} + \frac{V[1,n_y,i+1] + V[1,n_y,i-1]]}{{dl_z}^2} \right) \tag{A.18}$$

$$V[n_x,1,i] = \frac{dl_x^2 {dl_y}^2 {dl_z}^2}{2{dl_x}^2 {dl_y}^2 + {dl_x}^2 {dl_z}^2 + {dl_z}^2 {dl_y}^2} \left(\frac{V[n_x-1,1,i]}{dl_x^2} + \frac{V[n_x,2,i]}{dly^2} + \frac{V[n_x,1,i+1] + V[n_x,1,i-1]]}{{dl_z}^2} \right) \tag{A.19}$$

$$V[n_x,n_y,i] = \frac{dl_x^2 {dl_y}^2 {dl_z}^2}{2{dl_x}^2 {dl_y}^2 + {dl_x}^2 {dl_z}^2 + {dl_z}^2 {dl_y}^2} \left(\frac{V[n_x-1,n_y,i]}{dl_x^2} + \frac{V[n_x,n_y-1,i]}{{dl_y}^2} + \frac{V[n_x,n_y,i+1] + V[n_x,n_y,i-1]]}{{dl_z}^2} \right) \tag{A.20}$$

A.3 Faces

$$V[1,i,j] = \left(\frac{1}{dl_x^2} + \frac{2}{{dl_y}^2} + \frac{2}{dlz^2} \right) \left(\frac{V[2,i,j]}{dl_x^2} + \frac{V[1,i-1,j] + V[1,i+1,j]}{{dl_y}^2} + \frac{V[1,i,j-1] + V[1,i,j+1]}{{dl_z}^2} \right) \tag{A.21}$$

$$V[n_x,i,j] = \left(\frac{1}{dl_x^2} + \frac{2}{{dl_y}^2} + \frac{2}{{dl_z}^2} \right) \left(\frac{V[n_x-1,i,j]}{dl_x^2} + \frac{V[n_x,i-1,j] + V[n_x,i+1,j]}{{dl_y}^2} + \frac{V[n_x,i,j-1] + V[n_x,i,j+1]}{{dl_z}^2} \right) \tag{A.22}$$

$$V[j,1,i] = \left(\frac{2}{dl_x^2} + \frac{1}{dl_y{}^2} + \frac{2}{dl_z{}^2}\right)\left(\frac{V[j-1,1,i]+V[j+1,1,i]}{dl_x^2} + \frac{V[j,2,i]}{dl_y{}^2} + \frac{V[j,1,i-1]+V[j,1,i+1]}{dl_z{}^2}\right) \tag{A.23}$$

$$V[j,n_x,i] = \left(\frac{2}{dl_x^2} + \frac{1}{dl_y{}^2} + \frac{2}{dl_z{}^2}\right)\left(\frac{V[j-1,n_x,i]+V[j+1,n_x,i]}{dl_x^2} + \frac{V[j,n_x-1,1]}{dl_y{}^2} + \frac{V[j,n_x,i-1]+V[j,n_x,i+1]}{dl_z{}^2}\right) \tag{A.24}$$

$$V[i,j,1] = \left(\frac{2}{dl_x^2} + \frac{2}{dl_y{}^2} + \frac{1}{dl_z{}^2}\right)\left(\frac{V[i-1,j,1]+V[i+1,j,1]}{dl_x^2} + \frac{V[i,j-1,1]+V[i,j+1,1]}{dl_y{}^2} + \frac{V[i,j,2]}{dl_z{}^2}\right) \tag{A.25}$$

$$V[i,j,n_z] = \left(\frac{2}{dl_x^2} + \frac{2}{dl_y{}^2} + \frac{1}{dl_z{}^2}\right)\left(\frac{V[i-1,j,n_z]+V[i+1,j,n_z]}{dl_x^2}\,\frac{V[i,j-1,n_z]+V[i,j+1,n_z]}{dl_y{}^2} + \frac{V[i,j,n_z-1]}{dl_z{}^2}\right) \tag{A.26}$$

A.4 Bulk:

$$V[i,j,k] = 2\sigma[i,j,k]\left(\frac{1}{dl_x^2} + \frac{1}{dl_y{}^2} + \frac{1}{dl_z{}^2}\right)(\sigma[i+1,j,k] + 4\sigma[i,j,k] - \sigma[i-1,j,k])\,(V[i+1,j,k]) + (\sigma[i-1,j,k] + 4\sigma[i,j,k] - \sigma[i+1,j,k])\left(\frac{V[i-1,j,k]}{4dl_x^2}\right) + (\sigma[i,j+1,k] + 4\sigma[i,j,k] - \sigma[i,j-1,k])\,(V[i,j+1,k]) + (\sigma[i,j-1,k] + 4\sigma[i,j,k] - \sigma[i,j+1,k])\left(\frac{V[i,j-1,k]}{4dl_y{}^2}\right) + (\sigma[i,j,k+1] + 4\sigma[i,j,k] - \sigma[i,j,k-1])\,(V[i,j,k+1]) + (\sigma[i,j,k-1] + 4\sigma[i,j,k] - \sigma[i,j,k+1])\left(\frac{V[i,j,k-1]}{4dl_z{}^2}\right) \tag{A.27}$$

The total current is calculated across a section in the middle of the sample,

$$\text{current}_{total} = \sum_{ij}(\sigma[i,j,6](V[i,j,6] - V[i,j,5]))dl_x dl_y \tag{A.28}$$